nature

https://doi.org/10.1038/s41586-024-08315-x

Accelerated Article Preview

Evolving antibody response to SARS-CoV-2 antigenic shift from XBB to JN.1

Received: 18 June 2024

Accepted: 30 October 2024

Accelerated Article Preview

Cite this article as: Jian, F. et al. Evolving antibody response to SARS-CoV-2 antigenic shift from XBB to JN.1. *Nature* https://doi.org/10.1038/s41586-024-08315-x (2024)

Fanchong Jian, Jing Wang, Ayijiang Yisimayi, Weiliang Song, Yanli Xu, Xiaosu Chen, Xiao Niu, Sijie Yang, Yuanling Yu, Peng Wang, Haiyan Sun, Lingling Yu, Jing Wang, Yao Wang, Ran An, Wenjing Wang, Miaomiao Ma, Tianhe Xiao, Qingqing Gu, Fei Shao, Youchun Wang, Zhongyang Shen, Ronghua Jin & Yunlong Cao

Evolving antibody response to SARS-CoV-2 antigenic shift from XBB to JN.1

Fanchong Jian[1,2,3,#], Jing Wang[1,2,4,#], Ayijiang Yisimayi[1,2,4,#], Weiliang Song[1,2,4,#], Yanli Xu[5,#], Xiaosu Chen[6], Xiao Niu[1,3], Sijie Yang[1,7], Yuanling Yu[2], Peng Wang[2] ,Haiyan Sun[2], Lingling Yu[2], Jing Wang[2], Yao Wang[2], Ran An[2], Wenjing Wang[2], Miaomiao Ma[2], Tianhe Xiao[1,8], Qingqing Gu[2], Fei Shao[2], Youchun Wang[2,9], Zhongyang Shen[10], Ronghua Jin[5], Yunlong Cao[1,2,7*]

[1]Biomedical Pioneering Innovation Center (BIOPIC), Peking University, Beijing, China.

[2]Changping Laboratory, Beijing, China.

[3]College of Chemistry and Molecular Engineering, Peking University, Beijing, China.

[4]School of Life Sciences, Peking University, Beijing, China.

[5]Beijing Ditan Hospital, Capital Medical University, Beijing, China.

[6]Institute for Immunology, College of Life Sciences, Nankai University, Tianjin, China.

[7]Peking-Tsinghua Center for Life Sciences, Tsinghua University, Beijing, China.

[8]Joint Graduate Program of Peking-Tsinghua-NIBS, Academy for Advanced Interdisciplinary Studies, Peking University, Beijing, China.

[9]Institute of Medical Biology, Chinese Academy of Medical Science & Peking Union Medical College, Kunming, China.

[10]Organ Transplant Center, NHC Key Laboratory for Critical Care Medicine, Tianjin First Central Hospital, Nankai University, Tianjin, China.

[*]Correspondence: Yunlong Cao (yunlongcao@pku.edu.cn).

[#]These authors contributed equally.

Abstract

The continuous evolution of SARS-CoV-2, particularly the emergence of BA.2.86/JN.1 lineage replacing XBB, necessitates re-evaluation of vaccine compositions [1–3]. Here, we provide a comprehensive analysis of the humoral immune response to XBB and JN.1 human exposure. We demonstrate the antigenic distinctiveness of XBB and JN.1 lineages in SARS-CoV-2-naive individuals, and JN.1 infection elicits superior plasma neutralization against its subvariants. We highlight KP.3's strong immune evasion and receptor binding capability, supporting its foreseeable prevalence. Extensive analysis of the BCR repertoire, isolating ~2000 RBD-specific antibodies with their targeting epitopes characterized by deep mutational scanning (DMS), underscores the superiority of JN.1-elicited memory B cells [4,5]. Class 1 IGHV3-53/3-66-derived neutralizing antibodies (NAbs) contribute majorly within wildtype-reactive NAbs against JN.1. However, KP.2 and KP.3 evade a substantial subset, even those induced by JN.1, advocating for booster updates to KP.2/KP.3. JN.1-induced Omicron-specific antibodies also demonstrate high potency across Omicron. Escape hotspots of these NAbs have already been mutated, resulting in higher immune barrier to escape, considering probable recovery of escaped NAbs. Additionally, the prevalence of IGHV3-53/3-66-derived antibodies, and their capability of competing with all Omicron-specific NAbs suggests their inhibitory role on the activation of Omicron-specific naive B cells, potentially explaining the heavy immune imprinting in mRNA-vaccinated individuals [6–8]. These findings delineate the evolving antibody response to Omicron antigenic shift from XBB to JN.1, and highlight the importance of developing JN.1-lineage, especially KP.2/KP.3-based vaccine boosters.

Main

Since the emergence of the SARS-CoV-2 BA.2.86 lineage in July 2023, its subvariants, especially JN.1, have continued to circulate and evolve rapidly, outcompeting the previously prevalent XBB subvariants [1,3,9–11]. By June 2024, the JN.1 lineage accounted for over 93% of newly observed sequences (Fig. 1a). Importantly, BA.2.86 and JN.1 have convergently accumulated mutations on the receptor-binding domain (RBD) of the viral spike glycoprotein, including R346S/T, F456L/V, and A475V/S (Extended Data Fig. 1a) [12,13]. A newly detected subvariant, designated as KP.3, even carries an unprecedented Q493E mutation [14,15]. Most of these sites mutated in JN.1 subvariants are located near the receptor-binding motif (RBM) (Extended Data Fig. 1b). This makes it crucial to investigate their capabilities of evading the current humoral immune barrier established by SARS-CoV-2 infections and vaccines.

Previous studies demonstrated the capability of eliciting JN.1-effective NAbs of XBB-based vaccine boosters [16,17,2]. However, considering the extensive mutations carried by JN.1, it is important to investigate whether JN.1 immunization performs substantially better against current and potential future variants [1,3,18]. Here in this manuscript, we provided a systematic comparison of the humoral immune response between XBB and JN.1 lineages in human infections at both serum and MBC-encoded antibody resolution.

Results

Immunogenicity of JN.1 exposure

To evaluate the antigenicity and immunogenicity of the XBB and JN.1 lineages, we first administered a two-dose immunization of variant Spike mRNA in naïve mice (Extended Data Fig. 2a). Our observations revealed a pronounced distinction in antigenicity between the XBB and JN.1 lineages (Fig. 1b and Extended Data Fig. 2b). Notably, within the JN.1 family, KP.3 showed considerable antigenicity difference than JN.1 and KP.2, even when immunizing with KP.2 spike. These distinctions in antigenicity, at least in naive mice, prompts the consideration of changing SARS-CoV-2 vaccine compositions from XBB to JN.1 families.

Future SARS-CoV-2 variant prevalence is a critical guidance for vaccine composition assessment. Human ACE2 (hACE2)-binding affinity of viral RBDs is highly related to viral fitness, and previous studies have highlighted the synergistic impact of RBD L455-F456 mutations on ACE2 receptor binding affinity mediated by Q493 [12,19–22]. Given these sites are also convergently mutated in BA.2.86 lineages especially JN.1, we tested the binding affinities of JN.1 subvariant RBD to hACE2 using surface plasmon resonance (SPR) (Extended Data Fig. 1c). L455S in JN.1 dampens the high affinity of BA.2.86 RBD, as shown previously [1,23]. Importantly, F456L and R346T + F456L did not largely affect the hACE2-binding affinity of JN.1, while the Q493E mutation of KP.3 substantially improved the receptor binding affinity on the basis of JN.1 + F456L (Fig. 1c and Extended Data Fig. 1d). Interestingly, Q493E alone significantly reduces the ACE2 binding affinity in the context of JN.1 RBD, but unexpectedly enhances the affinity when combined with the F456L mutation, which indicates non-additive epistatic interactions (Fig. 1d) [12,24,25]. The high affinity of KP.3, achieved through epistasis, may enable the incorporation of A475V for further immune evasion (Fig. 1c). Overall, the extraordinary ACE2-binding affinity may bolster the rapid transmission and prevalence of KP.3, enhancing its potential to acquire additional immune-evasive mutations.

Human serum antibody evasion is the most deciding factor regarding SARS-CoV-2 viral fitness. To analyze the humoral immune evasion capability and immunogenicity of JN.1 lineages, we collected blood samples from 8 cohorts, including individuals infected by XBB* (n=11) or JN.1 (n=4) without known previous exposure to SARS-CoV-2, those who experienced XBB infection after 3 doses of inactivated vaccines, those who experienced sequential infections of BA.5/BF.7 and XBB* (n=14), or BA.5/BF.7 and JN.1 (n=29), and those who received 3-dose inactivated vaccines followed by BA.5/BF.7 breakthrough infection (BTI) and then reinfected by XBB (mainly XBB + S486P), HK.3, or JN.1 (n=54, 18, 29, respectively) (Fig. 2a and Extended Data Fig. 3).

Priming with XBB and JN.1 in naïve humans elicited distinct NAbs without observable cross-lineage reactivity, which confirms that XBB and JN.1 and antigenically distinct in both human and mice, indicating that antigenic change from XBB to JN.1 lineage results in different serotypes (Fig. 2b) [26,27]. In contrast, a prior BA.5 (or BF.7, omitted hereafter) infection improved the cross-lineage reactivity of antibodies induced by XBB or JN.1 reinfection. This suggests that BA.5/BF.7 priming could induce Omicron cross-reactive NAbs that are effective against both XBB and JN.1 lineages

(Fig. 2c).

Notably, in the three BTI with reinfection cohorts, "BA.5 BTI + XBB infection" elicited the lowest NT_{50} against JN.1 lineage variants (Fig. 2d). On average, JN.1 reinfection induced 5.9-fold higher NT_{50} against JN.1, 4.9-fold higher NT_{50} against KP.2, and 4.8-fold higher NT_{50} against KP.3, compared with XBB reinfection (Fig. 2e). The improvement of JN.1 BTI over HK.3 BTI was less significant, possibly due to the shorter interval between two infections in the XBB reinfection cohort, in addition to the immunogenicity drift attributed to the "FLip" mutations (L455F + F456L) of HK.3.

Among all five reinfection cohorts, all of the four tested JN.1 subvariants with RBD mutations, including JN.1 + R346T, JN.1 + F456L, KP.2, and KP.3, exhibited notable immune evasion. KP.3 consistently acted as the strongest escaper, leading to a 1.9 to 2.4-fold reduction in NT_{50} compared to JN.1. Importantly, a recently emerged deletion on NTD S31, which leads to N30 glycosylation and was convergently detected in multiple independent JN.1 sublineages including KP.2.3, LB.1, KP.3.1.1, and LF.2, results in further antibody evasion in all cohorts (Fig. 2c-d and Extended Data Fig. 3) [28].

Antigenic cartography of our human plasma neutralization data visualized the antigenic differences of SARS-CoV-2 variants. The antigenic map from single-exposure cohorts clearly depicted the intrinsic antigenic distances between XBB and JN.1 lineage in human, despite sample size limitations (Fig. 2f). Samples from BTI with reinfection cohorts showed strong ancestral strain imprinting, indicated by the aggregation of points near the D614G strain (Fig. 2g). Nevertheless, the JN.1 BTI cohorts displayed closer distance to current circulating variants, supporting the idea of switching vaccine boosters to JN.1 lineages.

Together, these observations underscore the significant antigenic distinctions between the SARS-CoV-2 XBB and JN.1 lineages, and highlight the notable ACE2 affinity and NAb-escaping capability of emerging JN.1 subvariants, especially KP.3 and KP.3 + S31del (KP.3.1.1), supporting their foreseeable prevalence. The results provide phenomenological but compelling evidence to shift the focus of vaccine booster strategies from XBB to JN.1 lineages, ideally KP.3.

JN.1-induced memory B cell repertoire

Then, we aim to dissect the specific molecular constituents responsible for the broad-spectrum neutralization observed in the plasma polyclonal antibodies (pAbs) elicited by infections with the JN.1 lineage, which would enable us to understand how prior vaccination or infection with BA.5 facilitates the development of cross-lineage NAbs following infections with XBB/JN.1. Analyzing the MBC repertoire could also help to predict the response to future variant exposures. Consequently, it is imperative and compelling to deconvolute the roles of antibodies that exhibit diverse cross-reactivities and target multiple epitopes, particularly on the virus RBD, the most immunogenic domain targeted by NAbs.

Therefore, we employed fluorescence-activated cell sorting (FACS) to isolate RBD-specific $CD20^+$ $CD27^+$ IgM^- IgD^- B cells using fluorescence activated cell sorting (FACS) from the peripheral blood mononuclear cells (PBMCs) of the human donors mentioned above. We utilized variant RBDs (XBB.1.5, HK.3, or JN.1) corresponding to the last-exposure SARS-CoV-2 strain for each cohort in the sorting (Supplementary Information Fig. 1). Following our previously established methodology, we determined the sequences of the mAb heavy and light chain variable domains using single-cell V(D)J sequencing (scVDJ-seq) and expressed them as human IgG1 [4,5,8,29,30]. The resultant mAbs were characterized using enzyme-linked immunosorbent assays (ELISA) to assess their binding specificities against the WT and the corresponding Omicron RBDs.

BA.5 BTI + reinfection consistently induced higher plasma neutralization titers against BA.5 compared to those against D614G, demonstrating the substantial contribution of Omicron-specific NAbs (Fig. 2d). This is validated by mAb analyses, in alignment with our earlier discovery that repeated Omicron infections may mitigate the imprinting of inactivated vaccines based on the ancestral strain [8]. However, recent research involving individuals who underwent Omicron reinfection after receiving mRNA vaccines based on the ancestral strain revealed pronounced immune imprinting; as a result, Omicron-specific MBCs were scarcely detectable even after two exposures to Omicron [6,7,31].

The XBB BTI cohort, comprising convalescents who underwent a single Omicron exposure post-vaccination, exhibits the highest proportion (62%) of RBD-specific mAbs that cross-react with the WT. Intriguingly, some vaccine-naïve cohorts, including XBB infection, BA.5 + XBB infection,

and BA.5 + JN.1 infection, also generate 40-50% WT-reactive antibodies. The BA.5 + JN.1 infection cohort induces a higher percentage of WT-reactive mAbs compared to the BA.5 BTI + JN.1 infection (Fig. 3a). However, the corresponding plasma samples did not display elevated neutralization titers against the D614G pseudovirus, suggesting an enrichment of cross-reactive mAbs that target non-neutralizing epitopes (Fig. 2c).

We observed substantial variations in V(D)J gene usage among the mAbs with different reactivities to WT and elicited by different immune histories. In the BA.5 BTI + reinfection cohorts, there is a prominent usage of IGHV3-53/3-66 in WT-reactive mAbs, which are recognized for being part of the public immune response and predominantly Class 1 NAbs targeting the RBM [30,32]. However, this type of mAbs is scarcely seen in cohorts without vaccination, where there is a higher utilization of IGHV5-51 and IGHV4-39 (Extended Data Fig. 4a). Regarding Omicron-specific mAbs, IGHV2-5 is prevalent across all cohorts, yet interestingly, it is not dominant among JN.1-infected convalescents, who show a higher proportion of mAbs derived from IGHV5-51 (Extended Data Fig. 4b). Notably, IGHV5-51 is also extensively used in WT-reactive antibodies, underscoring its significance, particularly in the context of JN.1 infections.

As expected, the rates of somatic hypermutation (SHM) in both the heavy and light chains of mAbs are closely associated with the number of antigen exposures. Specifically, WT-reactive mAbs exhibit more SHMs than Omicron-specific mAbs in vaccinated individuals, but not in unvaccinated ones. The cohorts BA.5 BTI + HK.3/JN.1 generate Omicron-specific mAbs with higher SHM rates compared to BA.5 BTI + XBB infection, likely due to the longer interval between two Omicron exposures in the former groups, allowing for further maturation of Omicron-specific B cells initiated by BA.5 infections (Fig. 3b and Extended Data Fig. 4c).

Generally, Omicron-specific mAbs demonstrated superior neutralization activities compared to WT-reactive mAbs against variants JN.1, KP.2, and KP.3. mAbs induced by XBB infection and XBB BTI displayed an exceedingly low percentage of potent NAbs, consistent with their low plasma neutralization titers (Fig. 2a and Extended Data Fig. 3a). Notably, BA.5 + JN.1 and BA.5 BTI + JN.1 infections elicited 30% and 60% JN.1-effective WT-reactive NAbs, respectively, while the proportion of effective Omicron-specific mAbs exceeded 90% in both cohorts, surpassing those

observed in XBB/HK.3 reinfections (Extended Data Fig. 4d). These findings further substantiate the potential benefits of developing vaccine boosters based on the JN.1 lineages.

Epitope mapping of JN.1-induced mAbs

Despite the promising neutralization activities of JN.1-elicited mAbs, antibodies targeting various epitopes may be evaded by diverse RBD mutations, suggesting their potential vulnerability to future viral antigenic drift. To examine the epitope distribution of mAbs elicited by different immune histories, we conducted high-throughput yeast-display-based DMS assays to analyze the escape mutation profiles of the isolated mAbs. Specifically, we constructed mutant libraries based on the XBB.1.5 and JN.1 RBDs. We initially assessed the expression levels of these mutants on the yeast surface using FACS followed by sequencing (Sort-seq) (Extended Data Fig. 5a-d) [14,15,33]. Interestingly, the expression of the JN.1 RBD appeared to be more tolerant to mutations compared to the BA.2 RBD, yet less tolerant than the XBB.1.5 RBD (Extended Data Fig. 5e). We then conducted DMS on the mAb binding capabilities to identify the escape mutations for each mAb, thereby mapping their targeting epitopes [8]. We successfully assayed the escape mutation profiles of a total of 2,688 mAbs, based on at least one of the two RBD variants, including 1,874 isolated from XBB/JN.1 infection cohorts involved in this study, and 814 mAbs previously identified for comparison (Extended Data Fig. 6a) [5,8,34,35].

We identified 22 mAb clusters, and the corresponding epitope groups for each cluster were annotated based on our previous definitions (Fig. 3c and Extended Data Fig. 6b) [5,8]. In brief, epitope groups A1/A2 (Class 1[32,36]), B (Class 1/2, similar to COV2-2196[37] and REGN10933[38]), D2/D3/D4 (similar to REGN10987[38] and LY-CoV1404[39]), and F3 (Class 1/4, similar to SA55[40] and ADG-2/VYD222[41]) generally compete with ACE2, and have a higher potential to effectively neutralize the virus. Conversely, groups E1/E2 (Class 3, S309-like), E3 (also referred to as “Class 5”, S2H97-like[42]), and F1 (Class 4, S304-like) are less likely to compete with ACE2 and do not exhibit potent neutralization (Fig. 3d and Extended Data Fig. 6c-d). Notably, we discovered a novel subgroup of F1, designated as F1.2, which targets an epitope adjacent to the traditional F1.1 but slightly closer to the RBM (Extended Data Fig. 6e).

We observe that the proportion of A1 mAbs correlates with the number of SARS-CoV-2 exposures, reaching highest levels in cohorts that experienced BTI followed by reinfection (Fig. 3e). These antibodies are notably absent in cases of XBB infection alone, underscoring the importance of initial exposure to earlier variants for the development of such mAbs. By differentiating F1.2 from F1.1, we deduce that WT-based vaccination is essential for eliciting traditional F1.1 non-neutralizing antibodies. In contrast, immunization solely with Omicron induces F1.2 mAbs only, which may be due to the immunogenicity shift caused by Omicron mutations at RBD positions 371-376. We also note that JN.1 infections do not elicit E1/E2 mAbs, which could be attributed to the N354 glycosylation resulting from K356T in the BA.2.86 lineage. Among the epitope groups, A1, D2, E1/E2/E3, and F1.1 are predominantly cross-reactive to WT; whereas A2, B, D3/D4, F1.2, and F3 primarily consist of Omicron-specific mAbs (Fig. 3f). Groups F3, A1, B, and D3 encompass potential bnAbs against JN.1 subvariants, whereas A2, D2, D4, and E1/E2.1 are largely escaped (Fig. 3g). E2.2/E3/F1.1 typically represent broadly reactive non-neutralizing antibodies. However, the novel F1.2 mAbs, which exhibited weak neutralization against SARS-CoV-2 variants prior to BA.2.86, demonstrate an unprecedentedly enhanced potency against JN.1 lineages (Fig. 3h). In addition, groups E1/E2.1, E2.2, F1.1, and F1.2 show a significant preference for light chain V genes, enriching for IGLV1-40, IGLV3-21, IGKV1-39, and IGLV6-57, respectively. Furthermore, E1/E2.1 and F1.1 tend to utilize IGHV1-69 and IGHV3-13/3-30 heavy chains, respectively, to pair with the corresponding light chains (Extended Data Fig. 6f).

Class 1 mAbs dominate WT-reactive bnAbs

Given the potential scarcity of Omicron-specific NAbs within the mRNA-vaccinated population, we then focus on the properties of WT-reactive mAbs elicited by three BA.5 BTI + reinfection cohorts. Consistent with the plasma neutralization and overall mAb neutralization analyses shown above, WT-reactive mAbs from HK.3 and JN.1 infections were significantly more effective than those from XBB infection against JN.1, KP.2, and KP.3 (Fig. 4a). We then calculated the "effectiveness scores" for each epitope group from each source cohort, defined as the number of mAbs in each epitope group weighted by their IC_{50} values against a specific variant. This metric helped us discern the contribution of each epitope group to neutralization (Fig. 4b). Notably, epitope group A1 consistently made a major contribution to the effectiveness against not only JN.1 but also

KP.2 and KP.3, which accumulate multiple mutations on the A1 epitope or even its escape hotspots, including L455S, F456L, and Q493E (Fig. 4b-c and Extended Data Fig. 6d).

As mentioned above, group A1 or Class 1 mAbs are predominantly derived from the IGHV3-53 or IGHV3-66 germline, which is well-known as public responses [30,32,43,44]. These mAbs tend to pair with the IGKV1-33 and IGKV3-20 light chain. A specific subset from BA.5 BTI + XBB reinfection cohort utilizes IGHV3-7 with IGKV1-NL1. The WT-reactive A1 mAbs from the three BTI + reinfection cohorts exhibit similar heavy chain SHM rates and similar neutralizing activities against XBB.1.5 and HK.3.1 (Fig. 4e-f). Nonetheless, those elicited by HK.3 and JN.1 demonstrate significantly enhanced neutralization against JN.1 subvariants. Notably, KP.2 and KP.3 evade (IC_{50} > 1 μg/mL) 31% and 52% of the mAbs elicited by XBB reinfection, respectively, but only 2% and 20% of the mAbs elicited by JN.1 reinfection. Compared to those elicited by XBB, JN.1-elicited A1 mAbs exhibit, on average, 7 to 10-fold higher neutralizing activity against JN.1, KP.2, and KP.3 (Fig. 4f and Extended Data Fig. 7a). Thus, in the context of WT-cross-reactive antibodies, JN.1 infection not only elicits higher neutralization against current JN.1-derived strains but also better enriches MBCs that encode effective Class 1 or epitope group A1 antibodies. Nevertheless, JN.1-elicited WT-reactive A1 NAbs exhibit a 3.2-fold and 10-fold reduction in reactivities against KP.2 and KP.3, respectively. Most strikingly, only 24% retain their neutralization against KP.3 + A475V (Fig. 4f). This susceptibility raises concerns regarding the effectiveness of JN.1 boosters in counteracting ongoing viral evolution, and indicates the need for vaccines derived from the KP.2/KP.3 lineage for robust protection against both current variants and future antigenic drifts.

We observed that the “broadly neutralizing” A1 mAbs do not exhibit significantly higher SHM rates and do not show significant preference in germline VDJ usage (Extended Data Fig. 7b-c) [45]. The escaped A1 mAbs exhibit higher DMS escape scores than the broadly neutralizing A1 mAbs on the mutations of interest, such as 456L and 475V on both antigen basis, but 455S and 493E only on the XBB.1.5 basis (Extended Data Fig. 7d-e). Previous structural analyses indicated that IGHV3-53/3-66 mAbs primarily utilize their CDR-H1 and part of CDR-H3 to interact with RBD residue A475; however, we did not observe notable differences in CDR-H1 patterns (Extended Data Fig. 7f) [10,43]. Therefore, we hypothesize that these A1 bnAbs rely on a distinctive core CDR-H3 and highly matured light chain for broad neutralization, as suggested by the preferences in IGHD gene usage

(Extended Data Fig. 7g-h).

Recent growth advantages of JN.1 subvariants with mutations on A1 epitope indicate the remarkable abundance of such NAbs within the global population. This is also revealed by assessing the average immune pressure by aggregating DMS profiles of WT-reactive mAbs from reinfection cohorts using a neutralization-weighted, codon-aware strategy, as described previously [5,8]. Despite the accumulation of escape mutations on the A1 epitope and the verified significant evasion, the retained A1 bnAbs still exert pressure on residues within its epitope hotspots, such as 403, 420, 455, 475, and 493 (Fig 4g-i). Unsurprisingly, the F456L mutation in KP.2 and KP.3 eliminates the L456 hotspot observed in JN.1 weighting; however, the score on residue E493 is even more pronounced in KP.3 weighting, as this mutation enables four new one-nucleotide-accessible amino acid mutations at this site, including Ala, Asp, Gly, and Val.

In summary, within the WT-reactive NAbs, epitope group A1 remains the most pronounced against JN.1 subvariants, despite multiple evasive mutations on its epitope during recent viral evolution. Therefore, the development of boosters based on JN.1, or even JN.1 + F456L, KP.2, or KP.3, should be considered to better elicit bnAbs and enrich for effective MBCs that can resist potential future immune escape mutations, particularly in individuals receiving mRNA vaccines, whose immune responses predominantly elicit WT-reactive antibodies.

Potential of Omicron-specific NAbs

Unlike mRNA vaccination, immune imprinting caused by inactivated vaccines appears to be mitigated by Omicron reinfection, which elicits a substantial amount of Omicron-specific antibody. As global vaccination strategies shift away from WT components and update to the latest variants, such mAbs may become the primary contributors to immune pressure in the future. Notably, JN.1 infection also induces Omicron-specific NAbs with significantly enhanced neutralization breadth against the JN.1 lineage compared to XBB or HK.3 infections (Fig. 5a). Epitope group F3 stands out as the most remarkable for broad neutralization, while A2, B, D3, and F1.2 also make minor contributions (Fig. 5b). A2 NAbs are likely to be evaded due to their highly overlapping epitope with group A1. Interestingly, groups B and D3 include both WT-reactive and non-reactive bnAbs

(Fig. 4b and 5b). Unsurprisingly, BTI cohorts elicit more WT-reactive B/D3 mAbs than unvaccinated cohorts, and these cross-reactive B/D3 mAbs exhibit a higher SHM rate than Omicron-specific ones (Extended Data Fig. 8a-b). Despite their cross-reactivity to WT, these antibodies demonstrate much higher neutralization activities against BA.5 compared to D614G, indicating potential Omicron-adaptive maturation (Extended Data Fig. 8c). WT-reactive and Omicron-specific B mAbs are derived from largely different heavy and light chain genes; however, D3 mAbs predominantly utilize IGHV5-51 regardless of their cross-reactivity (Extended Data Fig. 8d-e). Specific group B mAbs exhibit higher DMS escape scores on residues 478 and 486, and D3 higher on 440, which are mutated sites in Omicron lineages (Extended Data Fig. 8f-g). Many Omicron-specific B NAbs (but not D3) do not neutralize BA.1 and BA.2, which do not harbor the F486V/S/P mutations found in post-BA.5 variants, due to their vulnerability to 486 mutations (Extended Data Fig. 8h).

Despite the abundance of potent Omicron-specific NAbs in individuals who have experienced reinfection following prior inactivated vaccinations, we observed minimal evidence of mutations that enable escape from these NAbs. The lack of escape mutations against such NAbs is particularly notable in China, where the majority of the population has received inactivated vaccines combined with BA.5/BF.7 BTI, or even experienced more reinfections, suggesting weak selective pressure or inherent evolutionary constraints. Through the aggregation of DMS profiles of Omicron-specific NAbs, we have identified that all escape hotspots, except for G504, are located on residues of the RBD that have mutated in Omicron variant (Fig. 5c). Given the potential for neutralization recovery of previously escaped NAbs, these mutated sites may have a reduced likelihood for further mutation. Notably, mutations at G504 have been recently reported to enhance serum neutralization, likely due to their regulatory impact on the up-down dynamics of the Spike glycoprotein [46]. As anticipated, the four most prominent hotspots, encompassing residues 403, 405, 504, and 505, are all targeted by epitope F3 (Fig. 5d). Also, NAbs induced by JN.1 exhibit a remarkable breadth of neutralization against all tested JN.1 subvariants, outperforming those induced by XBB and HK.3 (Fig. 5e). This superiority is not surprising, as no additional mutations have occurred on their escape hotspots following the R403K mutation in BA.2.86. The SHM rates observed in HK.3 and JN.1-induced F3 mAbs are higher than those induced by XBB, inconsistent with the neutralization results which

show that XBB and HK.3 exhibit similar neutralization capabilities. This discrepancy suggests that maturation is not the predominant factor determining the broad neutralization efficacy of F3 (Fig. 5f).

Instead, F3 mAbs display intriguing patterns in the utilization of heavy and light chain V genes. F3 antibodies elicited by a single Omicron exposure, such as XBB infection and XBB BTI cohorts, are almost exclusively derived from the IGHV2-5 and IGKV3-15 pairing (Extended Data Fig. 9a). However, these NAbs exhibit weak neutralization against JN.1 lineages (Extended Data Fig. 9b). In contrast, repeated Omicron infections diversify the germline utilization of F3 mAbs, and generate F3 mAbs of comparable breadth regardless of vaccination (Fig. 5g and Extended Data Fig. 9c-d). Notably, JN.1 infection emphasizes the usage of IGHV5-51, particularly when paired with IGKV1-39. We demonstrate that, regardless of the source cohort, IGHV5-51 F3 antibodies are significantly more effective against JN.1 lineages than IGHV2-5-derived ones (Fig. 5h). However, we did not observe lower DMS scores on residue 403, which is intuitive given its presence in all BA.2.86 subvariants. Conversely, these IGHV5-51 F3 broad bnAbs exhibit higher escape scores on residues 405 and 504 (Fig. 5i). IGHV5-51 appears to be a noteworthy germline heavy chain V gene in the context of the antigenicity and immunogenicity of the JN.1 lineage. Specifically, IGHV5-51 encompasses three major epitope groups, E3, D3, and F3, with distinct patterns of light chain usage. E3 and F3 favor IGLV1-44 and IGKV1-39, respectively, while IGHV5-51 D3 mAbs utilize a wide range of light chain V genes (Extended Data Fig. 9e). The SHM rates of these groups do not show significant differences, and their neutralization capabilities closely align with the properties of their respective epitope groups (Extended Data Fig. 9f-g). These findings underscore the superior efficacy of JN.1-elicited Omicron-specific NAbs and emphasize the potency of these NAbs, especially the IGHV5-51-encoding F3 NAbs, against all Omicron variants, which should be considered as potential targets for the development of vaccines.

Clash of Class 1 and Omi-specific NAbs

Recent research has highlighted an exceptionally strong immune imprinting in individuals vaccinated with mRNA vaccines, as they fail to mount an Omicron-specific antibody response even following multiple Omicron exposures [6,7,31]. However, this phenomenon cannot be observed in

individual who received inactivated vaccines, or in mRNA-vaccinated mice [6,8]. Upon the comprehensive characterization of Omicron-specific antibodies, we surprisingly discovered that all Omicron-specific neutralizing epitopes on RBD compete with the A1 mAbs, which are well-known for the convergent usage of IGHV3-53/3-66 germline (Extended Data Fig. 10a-b). This competition was confirmed by SPR-based competition assays (Extended Data Fig. 10c). Given these results, we hypothesize that the presence of the IGHV3-53/3-66 convergent response is pivotal for this robust imprinting [47,48].

In essence, inactivated vaccines induce a weaker convergent response compared to mRNA vaccines. The individuals studied in our research experienced the "zero COVID" period in China during 2021-2022, leading to significant antibody waning. As a result, the concentration of Omicron-effective IGHV3-53/3-66 NAbs and corresponding MBCs may have been insufficient to effectively mask the antigen upon initial exposure to Omicron. This scenario would allow Omicron-specific naïve B cells to be activated and promoted to mature. These activated B cells could then be recalled by a subsequent Omicron exposure, leading to the generation of extensive Omicron-specific MBCs and antibodies. In contrast, the strong convergent responses in mRNA-vaccinated individuals may efficiently mask all Omicron-specific epitopes during the first Omicron encounter [49]. Their MBCs encoding effective IGHV3-53/3-66 public antibodies would be repeatedly activated with each Omicron exposure, demonstrating remarkable immune imprinting. Importantly, the ACE2-mimicking capability of these antibodies is also crucial, as it constrains viral evolution and ensures that these mAbs are not entirely evaded. Regarding mice, which lack the IGHV3-53/3-66 germline, they cannot generate a convergent response with a high amount of ACE2-mimicking NAbs, even if they are administered mRNA vaccines. It is important to note that these analyses are preliminary and intuitive, requiring further rigorous experimental validation (Extended Data Fig. 10d).

Discussion

The ongoing evolution of JN.1 subvariants, particularly those with mutations on the A1 epitope, which are more likely to impact receptor-binding capabilities and potentially cause epistatic effects, akin to those seen in KP.3, necessitates vigilant monitoring. We underscore the importance of V3-53/66 WT-reactive NAbs, which is also highlighted in a concurrent study [50]. We additionally point

out the potential of F3 Omicron-specific NAbs elicited by Omicron reinfection cohorts in achieving broad neutralization against the JN.1 lineage.

Although JN.1 infections elicit satisfactory cross-neutralization against its subvariants which support the efficacy of JN.1-based vaccine boosters, to enhance the generation of effective bnAbs against future antigenic drifts, it is advisable to consider developing future vaccine boosters based on KP.2/KP.3. For individuals who have received mRNA vaccines, the induction of WT-cross-reactive bnAbs in epitope group A1 through these boosters is particularly crucial for achieving broad-spectrum protection against both current and emerging SARS-CoV-2 variants. Additionally, if our hypothesis concerning the mechanism of heavy immune imprinting is validated, the use of a variant that demonstrates significant escape from A1 mAbs could potentially mitigate the effects of immune imprinting and effectively elicit Omicron-specific NAbs.

Acknowledgments

We thank all volunteers who provided blood samples. This study is financially supported by the Ministry of Science and Technology of China (2023YFC3043200), Changping Laboratory (2021A0201; 2021D0102), and National Natural Science Foundation of China (32222030; 2023011477).

Author Contributions

Y.C. designed and supervised the study. F.J. and Y.C. wrote the manuscript with inputs from all authors. A.Y., W.S., R.A., Yao W. and X.N. performed B cell sorting, single-cell VDJ sequencing experiments and data analysis. J.W. (BIOPIC), H.S., and F.J. performed and analyzed the DMS data. J.W. (Changping Laboratory) and F.S. performed the antibody expression and management. M.M. and W.W. constructed mRNA vaccines and conducted mouse immunization. Y.Y. and Youchun W. constructed the pseudotyped virus. P.W., L.Y., T.X. and W.W. performed the pseudovirus neutralization assays, ELISAs and SPR experiments. Q.G. proofread the manuscript. Y.X., X.C., Z.S. and R.J. recruited the patients.

Declaration of interests

Y.C. is listed as an inventor of provisional patent applications of SARS-CoV-2 RBD-specific antibodies. Y.C. is a co-founder of Singlomics Biopharmaceuticals. Other authors declare no competing interests.

Data availability

Information of mAbs involved in this study is included in the supplementary tables. Raw and processed DMS data and other necessary data related to this study can be downloaded from Zenedo (doi: 10.5281/zenodo.13893217).

Code availability

Custom scripts for reproduction the analyses in this study can be downloaded from Zenedo (doi: 10.5281/zenodo.13893217) and GitHub (https://github.com/yunlongcaolab/SARS-CoV-2-JN.1-mAbs).

Figure legend

Figure 1 | Antigenicity and receptor binding of emerging JN.1 subvariants

a, Dynamics of the percentage of XBB and JN.1 lineages in GISAID sequences from Sept 2023 to June 2024. **b**, Antigenic cartography of mouse sera neutralization data with SARS-CoV-2 variant Spike vaccination. Each square indicates a plasma sample and each circle indicates a SARS-CoV-2 variant. **c**, Barplots show the affinities of SARS-CoV-2 variants determined by SPR. Each circle indicates a replicate. Geometric mean K_D (nM) values are indicated by height of bars and annotated above each bar. **d**, Schematic for the non-additive ACE2 binding impacts between F456L and Q493E. The dashed gray arrows show the additive result.

Figure 2 | Antigenicity and immunogenicity comparison of XBB and JN.1 lineages in human

a, Schematic of the SARS-CoV-2-related immune histories of the seven cohorts involved in this study. **b-d**, 50% neutralization titers (NT_{50}) of plasma samples from seven different cohorts against SARS-CoV-2 variant pseudoviruses. Plasma source cohorts and corresponding number of samples are labeled above each panel. Dashed lines indicate the limit of detection (NT_{50} = 10). Numbers of

negative samples are labeled below the dashed lines. Geometric mean titers (GMT) values are labeled as black bars and shown above each group of points, with fold-changes and significance compared to JN.1 labeled. Two-tailed Wilcoxon signed-rank tests are used to calculate the p-values. **e**, Comparison of neutralization of plasma samples from three BTI + reinfection cohorts against KP.2 and KP.3. GMT values are labeled as black bars and above the points, with pair-wise fold-changes shown. Two-tailed Wilcoxon rank-sum tests are used to determine the p-values. *p<0.05; **p<0.01; ***p<0.001; ****p<0.0001; NS, not significant. **f-g**, Antigenic cartography performed using human plasma neutralization data of single-exposure cohorts (**f**) or ancestral strain imprinted cohorts (**g**). Each square indicates a plasma sample and each circle indicates a SARS-CoV-2 variant.

Figure 3 | Detailed characterization of XBB/JN.1-elicited mAbs

a, Proportion of WT-reactive and Omicron-specific mAbs isolated from different cohorts. Antibody reactivities were determined by ELISA against SARS-CoV-2 WT RBD and XBB.1.5, HK.3, or JN.1 RBD corresponding to the last-exposure variant. **b**, Distribution of heavy chain SHM rate of WT-reactive and Omicron-specific antibodies isolated from different cohorts. Number of mAbs are annotated above each violin plot. Two-tailed Wilcoxon rank-sum tests are used to calculate the p-values. NS, not significant. **c**, Uniform manifold approximation and projection (UMAP) visualization of antibody DMS escape mutation profiles. Well-known mAbs are highlighted by circles with names annotated. **d**, Schematic for the targeting sites of each epitope group on RBD. Epitope groups targeting spatially overlapped epitope are merged. **e**, Percentage of mAbs from each cohort in each epitope group. Number of epitope-characterized mAbs are labeled above the bars. **f**, Percentage of WT-reactive and Omicron-specific mAbs in each epitope group. **g-h**, Neutralization activities in IC_{50} of mAbs in each epitope group against D614G, XBB.1.5, JN.1, KP.2, and KP.3 pseudovirus. Number of mAbs in each group are shown in subtitles. Geometric mean IC_{50} (μg/mL) and percentage of mAbs with IC_{50} < 1 μg/mL are labeled above each group of points.

Figure 4 | Class 1 dominates WT-reactive bnAbs

a, Neutralization activities of WT-reactive mAbs isolated from three BTI + reinfection cohorts against JN.1, KP.2, and KP.3. Geometric mean IC_{50} (μg/mL) and percentage of mAbs with IC_{50} <

1 μg/mL are labeled above each group of points. **b**, Stacked bar charts show the effectiveness scores of WT-reactive mAbs in each epitope group weighted by IC_{50} against JN.1, KP.2, and KP.3. **c**, Average DMS site escape scores of mAbs in epitope groups A1, B, and D3. Hotspot residues are indicated by arrows. **d**, Chord diagram shows the heavy-light chain V gene pairing of mAbs in epitope group A1. The names of corresponding germline genes are annotated next to the strips. **e**, Comparison of heavy chain SHM rate of A1 mAbs elicited by BA.5 BTI + XBB, HK.3, and JN.1 reinfection cohorts. **f**, Neutralization activities of WT-reactive mAbs in epitope group A1 isolated from three BTI + reinfection cohorts. Geometric mean IC_{50} (μg/mL) and percentage of mAbs with $IC_{50} < 1$ μg/mL (red dashed lines) are labeled above each group of points. Black dash lines indicate limits of detection (0.005 and 10 μg/mL). **g-i**, Calculation of immune pressure on each RBD site and mutation based on the average of WT-reactive antibody escape mutation profiles weighted by JN.1 (**g**), KP.2 (**h**), KP.3 (**i**), and DMS for RBD expression and ACE2 binding. Hotspot residues are labeled and shown in logo plots. Two-tailed Wilcoxon rank-sum tests or signed-rank tests (first row, for paired samples) are used to determine the p-values. $^{***}p < 0.001$; $^{****}p < 0.0001$. ns, not significant.

Figure 5 | Broad neutralization of Omicron-specific NAbs

a, Neutralization activities of Omicron-specific mAbs isolated from three BTI + reinfection cohorts against JN.1, KP.2, and KP.3. Geometric mean IC_{50} (μg/mL) and percentage of mAbs with $IC_{50} <$ 1 μg/mL are labeled above each group of points. **b**, Stacked bar charts show the effectiveness scores of Omicron-specific mAbs each epitope group weighted by IC_{50} against JN.1, KP.2, and KP.3. **c**, Calculation of immune pressure on each RBD site and mutation based on the average of Omicron-specific antibody escape mutation profiles weighted by JN.1, and DMS for RBD expression and ACE2 binding. Hotspot residues are labeled and shown in logo plots. **d**, Average DMS site escape scores of mAbs in epitope group F3. Hotspot residues are indicated by arrows. **e**, Neutralization activities of Omicron-specific mAbs in group F3 isolated from BTI + reinfection cohorts. Geometric mean IC_{50} (μg/mL) and percentage of mAbs with $IC_{50} < 1$ μg/mL (red dashed lines) are labeled above each group of points. Black dash lines indicate limits of detection (0.005 and 10 μg/mL). **f**, Comparison of SHM rates of F3 mAbs elicited by BA.5 BTI + XBB, HK.3, and JN.1 reinfection cohorts. **g**, Chord diagram shows the heavy-light chain V gene pairing of mAbs isolated from BA.5

BTI + XBB/HK.3 or JN.1 in epitope group F3. **h**, Neutralization activities of Omicron-specific mAbs in group F3 isolated from BA.5 BTI + XBB/HK.3 or JN.1 cohort encoded by IGHV2-5 or IGHV5-51. **i**, Average DMS escape mutation scores of F3 mAbs encoded by IGHV2-5 or IGHV5-51.

References

1. Yang, S. *et al.* Fast evolution of SARS-CoV-2 BA.2.86 to JN.1 under heavy immune pressure. *Lancet Infect Dis* (2023) doi:10.1016/S1473-3099(23)00744-2.
2. Huiberts, A. J. *et al.* Effectiveness of Omicron XBB.1.5 vaccine against infection with SARS-CoV-2 Omicron XBB and JN.1 variants, prospective cohort study, the Netherlands, October 2023 to January 2024. *Eurosurveillance* **29**, 2400109 (2024).
3. Kaku, Y. *et al.* Virological characteristics of the SARS-CoV-2 JN.1 variant. *Lancet Infect Dis* (2024) doi:10.1016/S1473-3099(23)00813-7.
4. Cao, Y. *et al.* Omicron escapes the majority of existing SARS-CoV-2 neutralizing antibodies. *Nature* **602**, 657–663 (2022).
5. Cao, Y. *et al.* Imprinted SARS-CoV-2 humoral immunity induces convergent Omicron RBD evolution. *Nature* **614**, 521–529 (2023).
6. Liang, C.-Y. *et al.* Imprinting of serum neutralizing antibodies by Wuhan-1 mRNA vaccines. *Nature* 1–3 (2024) doi:10.1038/s41586-024-07539-1.
7. Tortorici, M. A. *et al.* Persistent immune imprinting occurs after vaccination with the COVID-19 XBB.1.5 mRNA booster in humans. *Immunity* **57**, 904-911.e4 (2024).
8. Yisimayi, A. *et al.* Repeated Omicron exposures override ancestral SARS-CoV-2 immune imprinting. *Nature* **625**, 148–156 (2024).
9. Yang, S. *et al.* Antigenicity and infectivity characterisation of SARS-CoV-2 BA.2.86. *The Lancet Infectious Diseases* **23**, e457–e459 (2023).
10. Liu, C. *et al.* A structure-function analysis shows SARS-CoV-2 BA.2.86 balances antibody escape and ACE2 affinity. *CR Med* **5**, (2024).
11. Yue, C. *et al.* ACE2 binding and antibody evasion in enhanced transmissibility of XBB.1.5. *The Lancet Infectious Diseases* **23**, 278–280 (2023).
12. Jian, F. *et al.* Convergent evolution of SARS-CoV-2 XBB lineages on receptor-binding domain 455–456 synergistically enhances antibody evasion and ACE2 binding. *PLOS Pathogens* **19**, e1011868 (2023).
13. Jian, F. *et al.* Further humoral immunity evasion of emerging SARS-CoV-2 BA.4 and BA.5 subvariants. *The Lancet Infectious Diseases* **22**, 1535–1537 (2022).
14. Starr, T. N. *et al.* Deep mutational scans for ACE2 binding, RBD expression, and antibody escape in the SARS-CoV-2 Omicron BA.1 and BA.2 receptor-binding domains. *PLOS Pathogens* **18**, e1010951 (2022).
15. Taylor, A. L. & Starr, T. N. Deep mutational scans of XBB.1.5 and BQ.1.1 reveal ongoing epistatic drift during SARS-CoV-2 evolution. *PLOS Pathogens* **19**, e1011901 (2023).
16. Wang, Q. *et al.* XBB.1.5 monovalent mRNA vaccine booster elicits robust neutralizing antibodies against XBB subvariants and JN.1. *Cell Host & Microbe* **32**, 315-321.e3 (2024).

17. Shilpi Jain *et al.* XBB.1.5 monovalent booster improves antibody binding and neutralization against emerging SARS-CoV-2 Omicron variants. *biorxiv* 2024.02.03.578771 (2024) doi:10.1101/2024.02.03.578771.
18. Planas, D. *et al.* Distinct evolution of SARS-CoV-2 Omicron XBB and BA.2.86/JN.1 lineages combining increased fitness and antibody evasion. *Nat Commun* **15**, 2254 (2024).
19. Carabelli, A. M. *et al.* SARS-CoV-2 variant biology: immune escape, transmission and fitness. *Nature Reviews Microbiology* **21**, 162–177 (2023).
20. Ma, W., Fu, H., Jian, F., Cao, Y. & Li, M. Immune evasion and ACE2 binding affinity contribute to SARS-CoV-2 evolution. *Nat Ecol Evol* **7**, 1457–1466 (2023).
21. Witte, L. *et al.* Epistasis lowers the genetic barrier to SARS-CoV-2 neutralizing antibody escape. *Nat Commun* **14**, 302 (2023).
22. Peng, R., Wu, L.-A., Wang, Q., Qi, J. & Gao, G. F. Cell entry by SARS-CoV-2. *Trends in Biochemical Sciences* **46**, 848–860 (2021).
23. Li, L. *et al.* Spike structures, receptor binding, and immune escape of recently circulating SARS-CoV-2 Omicron BA.2.86, JN.1, EG.5, EG.5.1, and HV.1 sub-variants. *Structure* **32**, 1055-1067.e6 (2024).
24. Starr, T. N. *et al.* Shifting mutational constraints in the SARS-CoV-2 receptor-binding domain during viral evolution. *Science* **377**, 420–424 (2022).
25. Taylor, A. L. & Starr, T. N. Deep mutational scanning of SARS-CoV-2 Omicron BA.2.86 and epistatic emergence of the KP.3 variant. 2024.07.23.604853 Preprint at https://doi.org/10.1101/2024.07.23.604853 (2024).
26. Simon-Loriere, E. & Schwartz, O. Towards SARS-CoV-2 serotypes? *Nat Rev Microbiol* **20**, 187–188 (2022).
27. Du, P. *et al.* The omicron BA.2.86 subvariant as a new serotype of SARS-CoV-2. *The Lancet Microbe* **5**, e516 (2024).
28. Cao, Y. *et al.* Characterization of the enhanced infectivity and antibody evasion of Omicron BA.2.75. *Cell Host Microbe* (2022) doi:10.1016/j.chom.2022.09.018.
29. Cao, Y. *et al.* BA.2.12.1, BA.4 and BA.5 escape antibodies elicited by Omicron infection. *Nature* **608**, 593–602 (2022).
30. Cao, Y. *et al.* Potent Neutralizing Antibodies against SARS-CoV-2 Identified by High-Throughput Single-Cell Sequencing of Convalescent Patients' B Cells. *Cell* **182**, 73-84 e16 (2020).
31. Addetia, A. *et al.* Neutralization, effector function and immune imprinting of Omicron variants. *Nature* **621**, 592–601 (2023).
32. Robbiani, D. F. *et al.* Convergent antibody responses to SARS-CoV-2 in convalescent individuals. *Nature* **584**, 437–442 (2020).
33. Starr, T. N. *et al.* Deep Mutational Scanning of SARS-CoV-2 Receptor Binding Domain Reveals Constraints on Folding and ACE2 Binding. *Cell* **182**, 1295-1310 e20 (2020).
34. Cao, Y. *et al.* Humoral immune response to circulating SARS-CoV-2 variants elicited by inactivated and RBD-subunit vaccines. *Cell Res* **31**, 732–741 (2021).
35. Cao, Y. *et al.* Humoral immunogenicity and reactogenicity of CoronaVac or ZF2001 booster after two doses of inactivated vaccine. *Cell Res* **32**, 107–109 (2022).
36. Barnes, C. O. *et al.* SARS-CoV-2 neutralizing antibody structures inform therapeutic strategies. *Nature* **588**, 682–687 (2020).
37. Loo, Y. M. *et al.* The SARS-CoV-2 monoclonal antibody combination, AZD7442, is protective

in nonhuman primates and has an extended half-life in humans. *Sci Transl Med* **14**, eabl8124 (2022).
38. Copin, R. *et al.* The monoclonal antibody combination REGEN-COV protects against SARS-CoV-2 mutational escape in preclinical and human studies. *Cell* **184**, 3949-3961 e11 (2021).
39. Westendorf, K. *et al.* LY-CoV1404 (bebtelovimab) potently neutralizes SARS-CoV-2 variants. *Cell Rep* **39**, 110812 (2022).
40. Cao, Y. *et al.* Rational identification of potent and broad sarbecovirus-neutralizing antibody cocktails from SARS convalescents. *Cell Rep* **41**, 111845 (2022).
41. Rappazzo, C. G. *et al.* Broad and potent activity against SARS-like viruses by an engineered human monoclonal antibody. *Science* **371**, 823–829 (2021).
42. Starr, T. N. *et al.* SARS-CoV-2 RBD antibodies that maximize breadth and resistance to escape. *Nature* **597**, 97–102 (2021).
43. Yuan, M. *et al.* Structural basis of a shared antibody response to SARS-CoV-2. *Science* **369**, 1119–1123 (2020).
44. Zhang, Q. *et al.* Potent and protective IGHV3-53/3-66 public antibodies and their shared escape mutant on the spike of SARS-CoV-2. *Nat Commun* **12**, 4210 (2021).
45. Li, L. *et al.* Breakthrough infection elicits hypermutated IGHV3-53/3-66 public antibodies with broad and potent neutralizing activity against SARS-CoV-2 variants including the emerging EG.5 lineages. *PLOS Pathogens* **19**, e1011856 (2023).
46. Bernadeta Dadonaite *et al.* Full-spike deep mutational scanning helps predict the evolutionary success of SARS-CoV-2 clades. *biorxiv* 2023.11.13.566961 (2023) doi:10.1101/2023.11.13.566961.
47. Schaefer-Babajew, D. *et al.* Antibody feedback regulates immune memory after SARS-CoV-2 mRNA vaccination. *Nature* **613**, 735–742 (2023).
48. Bergström, J. J. E., Xu, H. & Heyman, B. Epitope-Specific Suppression of IgG Responses by Passively Administered Specific IgG: Evidence of Epitope Masking. *Front. Immunol.* **8**, (2017).
49. Wang, Z. *et al.* mRNA vaccine-elicited antibodies to SARS-CoV-2 and circulating variants. *Nature* **592**, 616–622 (2021).
50. Paciello, I. *et al.* B cell maturation restored ancestral germlines to control Omicron BA.2.86. *bioRxiv* 2024.03.03.583187 (2024) doi:10.1101/2024.03.03.583187.

Extended Data Figure legend

Extended Data Fig. 1 | Prevalence and convergent evolution of JN.1 lineage

a, Schematic for the convergent evolution of BA.2.86/JN.1 lineage. **b**, Key mutated sites of BA.2.86/JN.1 lineage are indicated on the XBB.1.5 RBD structural model (PDB: 8WRL). **c**, Barplots show the affinities of additional SARS-CoV-2 variants determined by SPR. **d**, SPR sensorgrams of selected SARS-CoV-2 variants shown in Fig. 1c. Representative results of replicates are shown. Geometric mean k_a, k_d, and K_D of all replicates are labeled.

Extended Data Fig. 2 | Distinct antigenicity of XBB and JN.1 in mice

a, Schematic for the mouse immunization experiments. **b**, Radar plots show the serum NT_{50} of mouse that received 2-dose WT, BA.1, BA.5, XBB, HK.3, BA.2.86, JN.1, KP.2, or SARS-CoV-1 Spike mRNA vaccine against eight representative SARS-CoV-2 variants.

Extended Data Fig. 3 | Plasma neutralization against SARS-CoV-2 variants

NT_{50} of plasma samples from all of the eight different cohorts against SARS-CoV-2 variant pseudoviruses. Plasma source cohorts and corresponding number of samples, with a schematic showing the immune history, are labeled above each panel. Dashed lines indicate the limit of detection (NT_{50} = 10). Numbers of negative samples are labeled below the dashed lines. Geometric mean titers (GMT) values are labeled as black bars and shown above each group of points. Data in Fig. 2 are displayed here again for comparison.

Extended Data Fig. 4 | Properties of WT-reactive and Omicron-specific mAbs

a-b, IGHV gene distribution of WT-cross-reactive (**a**) and Omicron-specific (**b**) mAbs isolated from the seven cohorts involved in this study. **c**, Distribution of light chain SHM rate of WT-reactive and Omicron-specific antibodies isolated from different cohorts. Number of mAbs are annotated above each violin plot. Two-tailed Wilcoxon rank-sum tests are used to calculate the p-values. NS, not significant. **d**, Neutralization against JN.1, KP.2, and KP.3. Geometric mean IC_{50} values are shown as circles and annotated above the points. Black dash lines indicate limits of detection (0.005 and 10 μg/mL). Red dashed lines indicate criteria for robust neutralization (1 μg/mL). Percentage of mAbs exhibiting robust neutralization are annotated below the points.

Extended Data Fig. 5 | Characterization of RBD DMS mutant libraries

a, Number of variants and detected single mutations in the mutant libraries involved in this study. **b**, FACS diagram for Sort-seq of JN.1 mutant library to determine RBD mutant expression levels. **c**, Heatmap shows the results of DMS on RBD expression from Sort-seq. **d**, Comparison of RBD expression DMS results from two JN.1 libraries. **e**, Comparison of RBD expression DMS results between JN.1 and BA.2 (left), JN.1 and XBB.1.5 (right).

Extended Data Fig. 6 | DMS-based clustering of RBD-specific mAbs

a, UMAP of mAbs colored by the corresponding RBD basis of DMS experiments. Some mAbs are tested in both antigen mutant libraries and the average results are used for analysis. **b**, Unsupervised clustering of DMS profiles. **c**, UMAP of mAbs colored by ACE2 competition level as determined by competition ELISA. **d**, Logo plots show average escape scores of each RBD mutation of mAbs in each epitope group. Amino acids are colored according to chemical properties. **e**, Structural model of XBB.1.5 RBD in complex of human ACE2 (PDB: 8WRL) with the key residues of epitope groups F1.1 and F1.2 highlighted. **f**, Chord diagram shows the heavy-light chain V gene pairing of mAbs isolated from in epitope groups E1/E2.1, E2.2, F1.1, and F1.2.

Extended Data Fig. 7 | Properties of WT-reactive mAbs in epitope group A1

a, Neutralization of WT-reactive mAbs in epitope group A1 from three BTI + reinfection cohorts against SARS-CoV-2 variants. Geometric mean IC_{50} values are shown as circles and annotated above the points. Black dash lines indicate limits of detection (0.005 and 10 μg/mL). Red dashed lines indicate criteria for robust neutralization (1 μg/mL). Percentage of mAbs exhibiting robust neutralization, and fold-changes compared to IC_{50} against JN.1 are annotated above the points. Two-tailed Wilcoxon signed-rank tests are used to determine the p-values. *p<0.05; **p<0.01; ***p<0.001; ****p<0.0001; NS, not significant. **b**, Distribution of SHM rate of WT-reactive broadly neutralizing (broadly against the six tested strains) and escaped A1 antibodies (evaded by at least one variant). Number of mAbs and median SHM rates are annotated above each violin plot. Two-tailed Wilcoxon rank-sum tests are used to determine the p-values. **c**, Chord diagram shows the heavy-light chain pairing of WT-reactive broadly neutralizing and escaped A1 antibodies. **d**, Comparison of DMS site escape scores using XBB.1.5 library and JN.1 library of mAbs in epitope group A1 which were assayed in both libraries. **e**, Comparison of DMS escape scores of WT-reactive broadly neutralizing and escaped A1 antibodies. **f**, CDR-H1 motifs of IGHV3-53/3-66-encoding WT-reactive broadly neutralizing and escaped A1 antibodies. **g-h**, Chord diagram shows the heavy chain V-D (**g**) or V-J (**h**) pairing of WT-reactive broadly neutralizing and escaped A1 antibodies.

Extended Data Fig. 8 | Properties of mAbs in epitope groups B and D3

a, Number of WT-cross-reactive and Omicron-specific mAbs in groups B and D3 from vaccinated and corresponding unvaccinated cohorts. The p-values is calculated using two-tailed hypergeometric test. **b**, Distribution of SHM rate of WT-reactive and Omicron-specific B/D3 antibodies. Number of mAbs are annotated above each violin plot. Two-tailed Wilcoxon rank-sum tests are used to determine the p-values. *p<0.05; **p<0.01; ***p<0.001; ****p<0.0001; ns, not significant. **c**, Neutralization of WT-reactive B and D3 mAbs against D614G, BA.5, XBB.1.5, and JN.1. Percentage of mAbs exhibiting robust neutralization, and fold-changes compared to IC_{50} against BA.5 are annotated above the points. **d-e**, Chord diagram shows the heavy-light chain pairing of WT-reactive and Omicron-specific B (**d**) or D3 (**e**) mAbs. **f-g**, Scatter plots (**f**) and logo plots (**g**) to compare the DMS escape scores of WT-reactive (cross) and Omicron-specific B/D3 mAbs. **h**, Neutralization of Omicron-specific B and D3 mAbs against SARS-CoV-2 variant pseudovirus. Black dash lines indicate limits of detection (0.005 and 10 μg/mL). Red dashed lines indicate criteria for robust neutralization (1 μg/mL). Percentage of mAbs exhibiting robust neutralization, and fold-changes compared to IC_{50} against JN.1 are annotated above the points. Two-tailed Wilcoxon signed-rank tests are used to determine the p-values. *p<0.05; **p<0.01; ***p<0.001; NS, not significant.

Extended Data Fig. 9 | Properties of F3 and IGHV5-51 mAbs

a, Chord diagram shows the heavy-light chain pairing of F3 mAbs elicited by XBB infection (left) and XBB BTI (right). **b**, Neutralization of F3 mAbs s elicited by XBB infection (left) and XBB BTI (right) against SARS-CoV-2 variant pseudovirus. **c**, Chord diagram shows the heavy-light chain pairing of F3 mAbs elicited by BA.5 + XBB infection (left) and BA,5 + JN.1 infection (right). **d**, Neutralization of F3 mAbs s elicited by BA.5 + XBB infection (left) and BA,5 + JN.1 infection (right) against SARS-CoV-2 variant pseudovirus. **e**, Relationship between light chain V genes and epitope groups of IGHV5-51-encoding mAbs. **f**, Comparison of heavy chain SHM rates of IGHV5-51-encoding mAbs in epitope groups D3, E3, and F3. **g**, Neutralization of IGHV5-51-encoding mAbs in various epitope groups against D614G, XBB.1.5, JN.1, KP.2, and KP.3 pseudovirus.

Extended Data Fig. 10 | Competition between Class 1 and Omicron-specific NAbs

a, Superimposed structural models of representative antibodies in epitope group A1 and Omicron-specific neutralizing epitope groups. **b**, Superimposed structural models of representative antibodies in epitope group A1 and WT-reactive epitope groups. **c**, Heatmap for pair-wised SPR competition scores of representative mAbs in various epitope groups on XBB.1.5 RBD. Results related to epitope group A1 are highlighted by blue rectangles. **d**, Schematic for the model to explain the mRNA vaccine-induced immune imprinting.

Supplementary Tables

Table S1 | Information of human donors involved in this study.

Table S2 | Information of mAbs involved in this study.

Methods

Plasma isolation

Blood samples were collected from individuals who had either recovered from or been re-infected with the SARS-CoV-2 Omicron BTI variant. This was conducted under the research protocol approved by the Beijing Ditan Hospital, affiliated with Capital Medical University (Ethics Committee Archiving No. LL-2021-024-02), the Tianjin Municipal Health Commission, and the Ethics Committee of Tianjin First Central Hospital (Ethics Committee Archiving No. 2022N045KY). All participants provided their agreement for the collection, storage, and use of their blood samples strictly for research purposes and the subsequent publication of related data.

SARS-CoV-2 infections were confirmed by either antigen or PCR tests. Specific strains of infections were inferred based on the sampling time when the corresponding strain was the majority of detected sequences in the region of sample collection. The interval between last exposure and sampling is 33 ±8.9 days (Mean±SD).

Patients in the re-infection group were initially infected with the BA.5/BF.7 variants in December 2022 in Beijing and Tianjin, China [51]. From December 1, 2022, to February 1, 2023, over 98% of the sequenced samples were identified as BA.5* (excluding BQ*), primarily consisting of the subtypes BA.5.2.48* and BF.7.14*, which were representative of the BA.5/BF.7 variants during this period. Subsequently, patients in the XBB BTI cohort and those with secondary infections in the re-infection group contracted the virus between May and June 2023. More than 90% of the sequenced samples from Beijing and Tianjin during this period corresponded to the XBB*+486P variant.

Plasma samples were isolated and tested for neutralization titers against SARS-CoV-2 variant spike-pseudotyped vesicular stomatitis virus (VSV). Whole blood was diluted in a 1:1 ratio with a solution of phosphate-buffered saline (PBS) supplemented with 2% fetal bovine serum (FBS). This was followed by Ficoll gradient centrifugation (Cytiva, 17-1440-03). After centrifugation, the plasma was collected from the upper layer, stored in aliquots at 20°C or lower, and heat-inactivated prior to subsequent experiments.

Pseudovirus preparation and neutralization

The SARS-CoV-2 variant spike protein pseudovirus was generated using the vesicular stomatitis virus (VSV) pseudovirus packaging system as described previously [8,52]. In addition to previously constructed variants, we additionally included “FLiRT”/KP.2 (JN.1 + R346T + F456L), KP.3 (JN.1 + F456L + Q493E), and their subvariants with S31del (SARS-CoV-2 ancestral strain numbering). The spike protein gene was codon-optimized and integrated into the pcDNA3.1 expression plasmid via the BamHI and XbaI restriction enzyme sites to augment the expression efficiency of the spike protein in mammalian cells. During pseudovirus production, the 293T cells (American Type Culture Collection (ATCC, CRL-3216)) were transfected with the SARS-CoV-2 spike protein expression plasmid. Post-transfection, these cells were infected with the G*ΔG-VSV virus (VSV-G pseudotyped virus, Kerafast) present in the cell culture supernatant. The pseudovirus was subsequently harvested and filtered from the supernatant, aliquoted, and stored at -80°C for later use.

Pseudovirus neutralization assays were performed using the Huh-7 cell line (Japan Collection of

Research Bioresources [JCRB], 0403). Plasma samples were serially diluted and mixed with the pseudovirus. Following an incubation period of 1 hour at 37°C with 5% CO_2, digested Huh-7 cells were introduced and incubated for an additional 24 hours at 37°C. The supernatant was then removed, and the mixture was incubated with D-Luciferin reagent (PerkinElmer, 6066769) in darkness for 2 minutes. The cell lysate was transferred to a detection plate, and the luminescence intensity was measured using a microplate spectrophotometer (PerkinElmer, HH3400). NT_{50} values were determined using a four-parameter logistic regression model [53].

Surface plasmon resonance

SPR experiments were conducted on Biacore 8K (Cytiva) to determine the RBD-hACE2 binding affinities. Human ACE2-Fc was immobilized onto Protein A sensor chips (Cytiva). Purified SARS-CoV-2 variant RBD samples prepared in serial dilutions (6.25, 12.5, 25, 50, and 100 nM) were injected on the sensor chips. Response units were recorded by Biacore 8K Evaluation Software 3.0 (Cytiva) at room temperature. Raw response data were fitted to 1:1 binding models to determine the association and dissociation kinetic constants (k_a and k_d), and binding affinities (dissociation equilibrium constant KD) using Biacore 8K Evaluation Software 3.0 (Cytiva).

In the competitive binding assays, we employed anti-His-tagged CM5 sensor chips (Cytiva) to immobilize 5 μg/mL of the RBD protein for a duration of 1 minute. Subsequently, a concentration of 20 μg/mL of antibody 1 was introduced for 2 minutes, followed by the introduction of antibody 2 at the identical concentration and for the same duration. We utilized Glycine 1.5 for the regeneration phase.

mRNA vaccine preparation and mouse immunization

For mRNA vaccine preparation, 5′ untranslated region (UTR), target sequence, and 3′ UTR were sequentially integrated downstream of the T7 promoter within an empty PSP73 plasmid. Subsequently, a double-digestion process was employed to produce linearized DNA. This DNA served as a template for a T7 RNA polymerase-driven in vitro transcription process to generate RNA that encodes the SARS-CoV-2 S6P (F817P, A892P, A899P, A942P, K986P, V987P, R683A, and R685A) protein, according to the manufacturer's instructions (Vazyme, DD4201). The

transcriptional outputs underwent DNase I treatment for the elimination of DNA templates, followed by a purification step utilizing VAHTS RNA Clean Beads (Vazyme, N412-02). Cap 1 structure was added using Vaccinia Capping Enzyme (Vazyme, DD4109) and mRNA Cap 2′-O-methyltransferase (Vazyme, DD4110), with a subsequent purification via magnetic beads. The incorporation of Poly(A) tails was achieved with Escherichia coli Poly(A) Polymerase (Vazyme, N4111-02), culminating in another round of purification.

The mRNA was encapsulated in a functionalized lipid nanoparticle as described previously [54]. Concisely, a solution containing ionizable lipid, DSPC, cholesterol, and PEG2000-DMG was prepared in ethanol, maintaining a molar ratio of 50:10:38.5:1.5, respectively. The mRNA was then diluted in a 50 mM citrate buffer (pH 4.0), free of RNase, to achieve a final lipid:mRNA weight ratio of 6:1. The aqueous and ethanol solutions were mixed in a 3:1 volume ratio using a microfluidic apparatus and the obtained lipid nanoparticles were then subjected to overnight dialysis. To preserve the chemical stability of the components, all samples were stored at temperatures ranging from 2 to 8 °C for up to a week. The dimensions and distribution of particle sizes of the lipid nanoparticles, as well as the encapsulation efficiency and concentration of mRNA, were meticulously assessed, revealing encapsulation rates typically between 90% and 99%.

Animal experiments were carried out under study protocols approved by Rodent Experimental Animal Management Committee of Institute of Biophysics, Chinese Academy of Sciences (SYXK2023300) and Animal Welfare Ethics Committee of HFK Biologics (HFK-AP-20210930). 10 female BALB/c mice, aged between six to eight weeks, were used in each group. The number of animals is determined on the basis that differences between experimental groups could be confirmed. No randomization or blinding was performed. The mice were housed under a 12-hour light and 12-hour dark cycle, with room temperatures maintained between 20 °C and 26 °C and humidity levels maintained between 30% and 70%. mRNA vaccines were given intramuscularly at dosages of either 10 μg per mouse. Blood samples were collected 2 weeks after the final immunization, as shown in Extended Data Fig. 3a.

Antigen-specific cell sorting and single-cell V(D)J sequencing

PBMCs and plasma were isolated from blood samples using Ficoll (Cytiva, 17-1440-03) density

792 gradient centrifugation. B cells were enriched from PBMCs using the $CD19^+$ positive selection kit
793 (STEMCELL, 17854). The enriched B cells were then stained with RBD of the last infected variant
794 as well as the ancestral strain RBD. B cells were also stained with antibodies against CD20
795 (BioLegend, 302304), CD27 (BioLegend, 302824), IgM (BioLegend, 314532), and IgD
796 (BioLegend, 348210), and 7-AAD (Invitrogen, 00-6993-50).

797 B cells that were positive for last infected variant RBD (XBB.1.5, HK.3, or JN.1) and CD20, CD27,
798 but negative for IgM, IgD and 7-AAD, were sorted. These RBD-binding B cells were subsequently
799 subjected to single-cell V(D)J sequencing using the using the Chromium Next GEM Single Cell
800 V(D)J Reagent Kits v1.1 according to the manufacturer's user guide (10X Genomics, CG000208).

801 10X Genomics V(D)J Illumina sequencing data were assembled as BCR contigs and aligned to the
802 GRCh38 BCR reference using Cell Ranger (v6.1.1) pipeline. For quality control, only the
803 productive contigs and B cells with one heavy chain and one light chain were kept. The germline
804 V(D)J genes were identified and annotated using IgBlast (v1.17.1) [55]. SHM nucleotides and residues
805 in the antibody variable domain were detected using Change-O toolkit (v1.2.0) [56].

806 **Expression and purification of mAbs**

807 Antibody heavy and light chain genes were first optimized for human cell expression and
808 synthesized by GenScript. VH and VL segments were separately inserted into plasmids (pCMV3-
809 CH, pCMV3-CL or pCMV3-CK) through infusion (Vazyme, C112). Plasmids encoding heavy
810 chains and light chains of antibodies were co-transfected to DH5α chemically competent cells
811 (Tsingke, #TSC-C01-96), spread onto LB solid medium (Beyotime, #ST158) supplemented with
812 ampicillin (Solarbio, #A1170), and single colonies cultured overnight were selected for PCR
813 identification. Positive bacterial cultures were subjected to Sanger sequencing for verification.
814 Finally, positive clones were selected based on sequence alignment, expanded for culture, and
815 plasmid extraction (CWBIO #CW2105).

816 Expi-293F cells with a density of 0.3-0.35 × 10^6 cells/mL were subcultured into 20 mL of culture
817 medium (OPM Biosciences, #81075-001), sealed, and incubated at 37°C, 125 ± 5 rpm in an 8%
818 CO_2 atmosphere. When the cell density reached 2-3 × 10^6 cells/mL (typically in 3 days), the cells

were treated with medium to dilute the density to 2 × 10^6 cells/mL and cultured overnight. For transfection, the antibody-encoding plasmids was diluted with 0.9% NaCl solution, mixed with polyethylenimine (PEI) transfection reagent (Yeasen, #40816ES03), and added to the cell culture. The reaction bottle was then returned to the shaker and incubated at 37°C, 8% CO_2, and 125 ± 5 rpm. 24 hours after transfection, the matching feed solution (OPM Biosciences, #F081918-001) (1 mL/bottle) was added, and feeding was performed every other day for 6-10 days.

For antibody purification, the expression culture was centrifuged at 3000 g for 10 minutes to remove cells, and the supernatant was collected. Protein A Magnetic beads (GenScript, L00695) were added and incubated at room temperature for 2 hours, then transferred to a 24-well plate and purified using the KingFisher automated system (Thermo Fisher). The purified antibody protein was quantified using a Nanodrop (Thermo Fisher, #840-317400) and the purity confirmed by SDS-PAGE (LabLead, #P42015).

Enzyme-linked immunosorbent assays

SARS-CoV-2 XBB.1.5, HK.3, and JN.1 RBD were individually aliquoted into a 96-well plate and incubated overnight at 4°C. The plate was then washed three times with PBST (phosphate-buffered saline with Tween-20). Subsequently, the wells were blocked with 3-5% BSA (bovine serum albumin) in PBST at 37°C for 2 hours. After another three washes with PBST, 100 μL of 1 μg/mL antibodies were added to each well and incubated for 30 minutes at room temperature. The plate was washed five times to remove unbound antibodies. Peroxidase-conjugated AffiniPure Goat Anti-Human IgG(H+L) (JACKSON, 109-035-003) was added and incubated at room temperature for 15 minutes, followed by five washes with PBST. The substrate tetramethylbenzidine (TMB) (Solarbio, 54827-17-7) was added and incubated for 10 minutes. The enzymatic reaction was halted by the addition of 2 M H_2SO_4. Finally, the absorbance of each well was measured at 450 nm using a microplate reader (PerkinElmer, HH3400).

Construction of DMS libraries

Replicate DMS libraries spanning from N331 to T531 (Wuhan-Hu-1 reference numbering) of SARS-CoV-2 XBB.1.5 and JN.1 variants were constructed as outlined previously[1,2]. Initially, site-directed mutagenesis PCR with computationally designed NNS primers was conducted to generate

all potential amino acid mutations on XBB.1.5 and JN.1 RBD. Then, each RBD variant was tagged with a unique 26-nucleotide (N26) barcode via PCR and assembled into Yeast surface display vector (Addgene, 166782). The XBB.1.5 and JN.1 DMS libraries were further transfected into electrocompetent DH10B cells for plasmid amplification and proceed to PacBio sequencing library preparation to decipher the association between RBD variant and corresponding N26 barcode. These enlarged DMS libraries were introduced into the EBY100 strain of *Saccharomyces cerevisiae* and screened on SD-CAA agar plates and subsequently expanded in SD-CAA liquid media, which were further preserved at -80°C after being flash-frozen in liquid nitrogen.

Profiling of mutation effects on RBD expression

RBD expression profile for JN.1 DMS libraries was performed as previously described[2]. Briefly, yeast libraries were first recovered and propagated overnight at 30°C in SD-CAA from an original OD600 of 0.1. Then, RBD surface expression was induced by diluting the yeast cells back to SG-CAA at initial OD600 equals to 0.67 and incubating the yeasts at room temperature with mild shaking for 16 hours. Secondly, 45 OD units of induced yeasts were washed twice using PBSA (PBS supplemented with 0.2 mg/L bovine serum albumin, pH 7.4) and incubated with 1:100 diluted FITC conjugated anti-C-MYC antibody (Immunology Consultants Lab, CMYC-45F) for 1 hour at room temperature under gentle agitation. After washing with PBSA, these yeast cells were resuspended in PBSA for fluorescence-activated cell sorting (FACS). The above prepared yeasts were analyzed via BD FACSAria III cytometer by gating for single events and further partitioning into four bins according to FITC fluorescence intensity: bin 1 captured 99% of non-labelled cells while bin 2 to 4 equally divided the rest of yeasts. In total, over 25 million yeasts were collected across these four bins for each library. After sorting, yeasts from each collection tube were centrifuged for 5 minutes and resuspended in 5 mL SD-CAA. To quantify the yeast recovery rate after sorting, 10 μl of the post-sorting sample from each bin was further diluted and spread on YPD agar plates, the remaining samples were grown overnight and proceed to plasmid extraction, N26 barcode amplification and next generation sequencing.

MACS-based antibody mutation escape profiling

High-throughput mutation escape profiling for each mAb was conducted based on magnetic-

activated cell sorting (MACS) following previously reported method[1]. In brief, improperly folded RBD variants in XBB.1.5 and JN.1 DMS libraries were removed using ACE2 (Sino Biological, 10108-H08H-B) conjugated biotin binder beads (Thermo Fisher, 11533D). After washing with PBSA, the beads captured RBD expressing yeasts were released and enlarged in SD-CAA and then preserved as frozen aliquots at -80°C.

For MACS-based mutation escape profiling, the ACE2-binder yeasts were thawed in SD-CAA with shaking overnight and back-diluted into SG-CAA for RBD surface expression induction. Execution of two sequential rounds of negative selection with any given antibody eliminated specific antibody binders in libraries. Then MYC-tag-based positive selection was performed using anti-c-Myc magnetic beads (Thermo Fisher Scientific, 88843) to capture the RBD expressing yeasts in the antibody-escaping population after two rounds of negative selection.

Final obtained yeast population was washed and grown overnight in SD-CAA and submitted to plasmid extraction by 96-wells yeast plasmid extraction Kit (Coolaber, PE053). N26 barcode amplification was further conducted using obtained plasmid as the PCR template, further purified with 1X Ampure XP beads (Beckman Coulter, A63882) and subjected to single end sequencing.

Antibody DMS data analysis

The raw sequencing data from the directed mutagenesis screening (DMS) were processed as previously described [8,12]. Specifically, the barcode sequences detected from both the antibody-screened and reference libraries were aligned to a barcode-variant dictionary using alignparse (v0.6.2) and dms_variants (v1.4.3) tools, derived from PacBio sequencing data of the XBB.1.5 and JN.1 DMS libraries. Ambiguous barcodes were excluded during the merging of yeast libraries. Only barcodes detected more than five times in the reference library were considered for further analysis. The escape score for a variant X, present in both the screened and reference libraries, was calculated as $F \times (n_{X,ab} / N_{ab}) / (n_{X,ref} / N_{ref})$, where F is a scaling factor to normalize the scores to a 0-1 range, and n and N represent the number of detected barcodes for variant X and the total barcodes in the antibody-screened (ab) or reference (ref) samples, respectively. For antibodies subjected to DMS with multiple replicates using different mutant libraries, the final escape score for each mutation was averaged for subsequent analyses.

We employed graph-based unsupervised clustering and embedding to assign an epitope group to each antibody and visualize them in a two-dimensional space. Initially, site escape scores (sum of mutation escape scores per residue) for each antibody were normalized to a sum of one, representing a distribution over RBD residues. The dissimilarity between two antibodies was quantified by the square root of the Jensen-Shannon divergence of the normalized escape scores. Pairwise dissimilarities for all antibodies in the dataset were computed using the SciPy module (scipy.spatial.distance.jensenshannon, v1.7.0). A k-nearest-neighbor graph was constructed using the python-igraph module (v0.9.6), and Leiden clustering was applied to assign a cluster to each antibody [57]. Cluster names were manually annotated based on the characteristic sites in the average escape profiles of each cluster, aligning with the nomenclature of our previously published DMS dataset [8]. To visualize the dataset in 2D, UMAP was performed based on the constructed k-nearest-neighbor graph using the umap-learn module (v0.5.2), and figures were generated using the R package ggplot2 (v3.3.3).

To compute the average immune pressure or identify escape hotspots using a collection of mAb DMS profiles, we followed a similar approach as in our previous study, incorporating four types of weights to account for the impact of each mutation on hACE2-binding affinity, RBD expression, neutralizing activity, and codon constraints at each residue. Due to the absence of ACE2 binding DMS data on the JN.1 basis, we utilized XBB.1.5-based results to filter out ACE2-dampening mutations in our calculations, which may introduce artifacts when strong epistasis is present [5,8]. For codon usage constraints, mutations inaccessible through single nucleotide changes were assigned a weight of zero, while others received a weight of 1.0. We used JN.1 (EPI_ISL_18373905), KP.2 (EPI_ISL_18916251), and KP.3 (EPI_ISL_19036766) to define one-nucleotide-accessible amino acid mutations. Neutralizing activity weights were calculated as $-\log_{10}(IC_{50})$, with IC_{50} values below 0.0005 or above 1.0 adjusted to 0.0005 or 1.0, respectively. Raw escape scores for each antibody were normalized by the maximum score across all mutants. The weighted score for each antibody and mutation was obtained by multiplying the normalized scores by the corresponding four weights, and the final mutation-specific weighted score was the sum of scores for all antibodies in the designated set, subsequently normalized to a 0-1 range. To visualize the calculated escape maps, sequence logos were generated using the Python module logomaker (v0.8).

Methods References

51. Pan, Y. *et al.* Characterisation of SARS-CoV-2 variants in Beijing during 2022: an epidemiological and phylogenetic analysis. *The Lancet* **401**, 664–672 (2023).

52. Li, H. *et al.* Establishment of replication-competent vesicular stomatitis virus-based recombinant viruses suitable for SARS-CoV-2 entry and neutralization assays. *Emerg Microbes Infect* **9**, 2269–2277 (2020).

53. Nie, J. *et al.* Establishment and validation of a pseudovirus neutralization assay for SARS-CoV-2. *Emerg Microbes Infect* **9**, 680–686 (2020).

54. Yanez Arteta, M. *et al.* Successful reprogramming of cellular protein production through mRNA delivered by functionalized lipid nanoparticles. *Proceedings of the National Academy of Sciences* **115**, E3351–E3360 (2018).

55. Ye, J., Ma, N., Madden, T. L. & Ostell, J. M. IgBLAST: an immunoglobulin variable domain sequence analysis tool. *Nucleic Acids Res* **41**, W34-40 (2013).

56. Gupta, N. T. *et al.* Change-O: a toolkit for analyzing large-scale B cell immunoglobulin repertoire sequencing data. *Bioinformatics* **31**, 3356–8 (2015).

57. Traag, V. A., Waltman, L. & van Eck, N. J. From Louvain to Leiden: guaranteeing well-connected communities. *Scientific Reports* **9**, 5233 (2019).

Figure 1

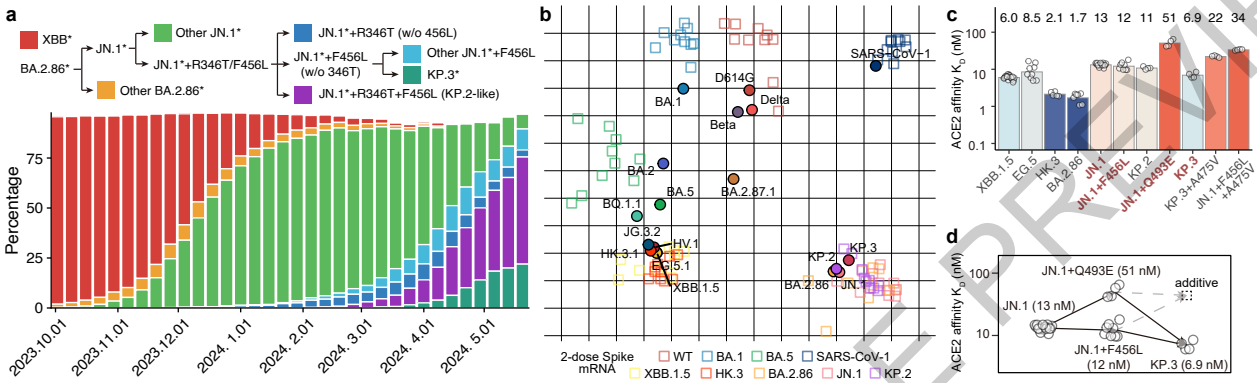

Figure 2

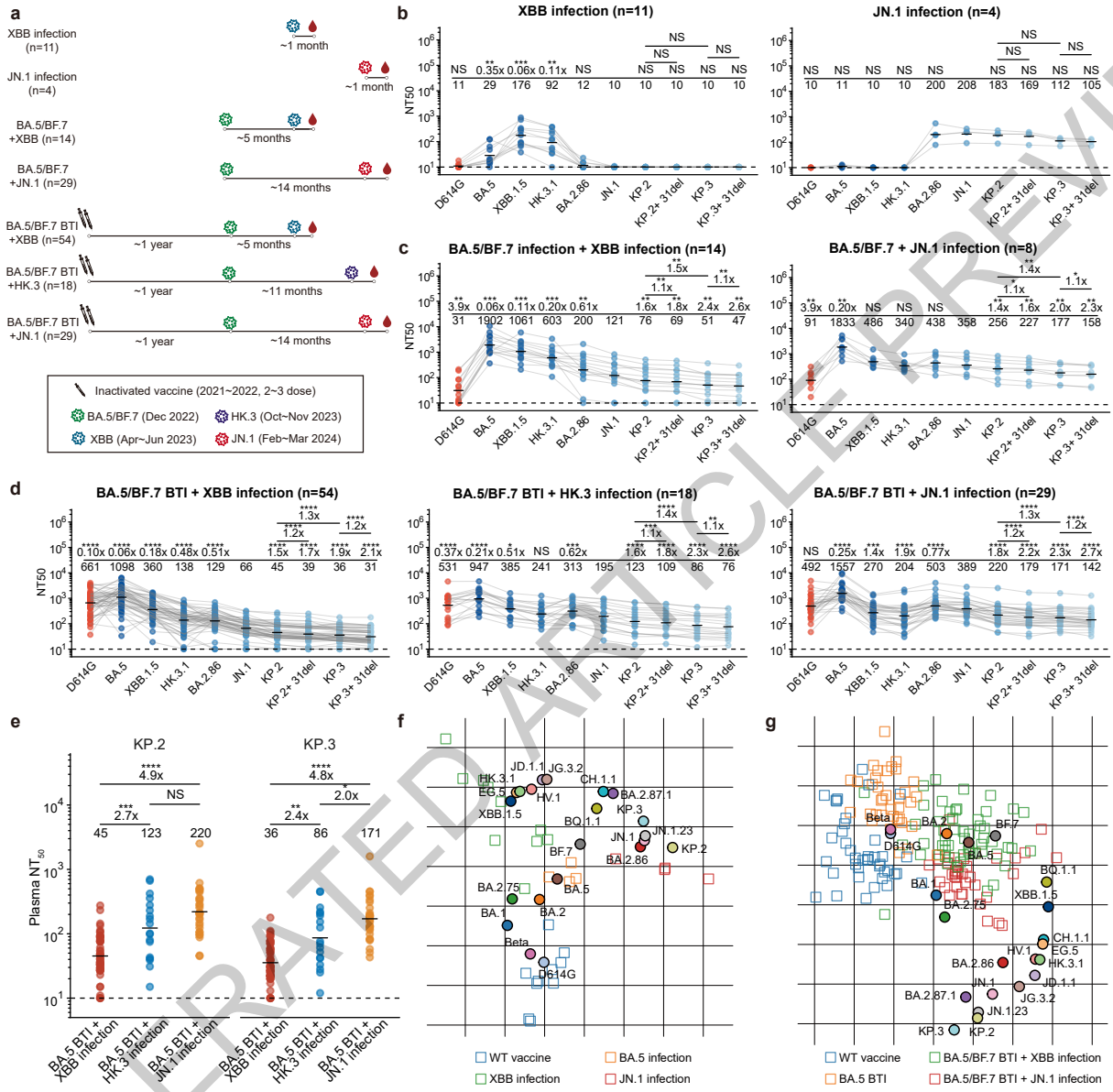

Figure 3

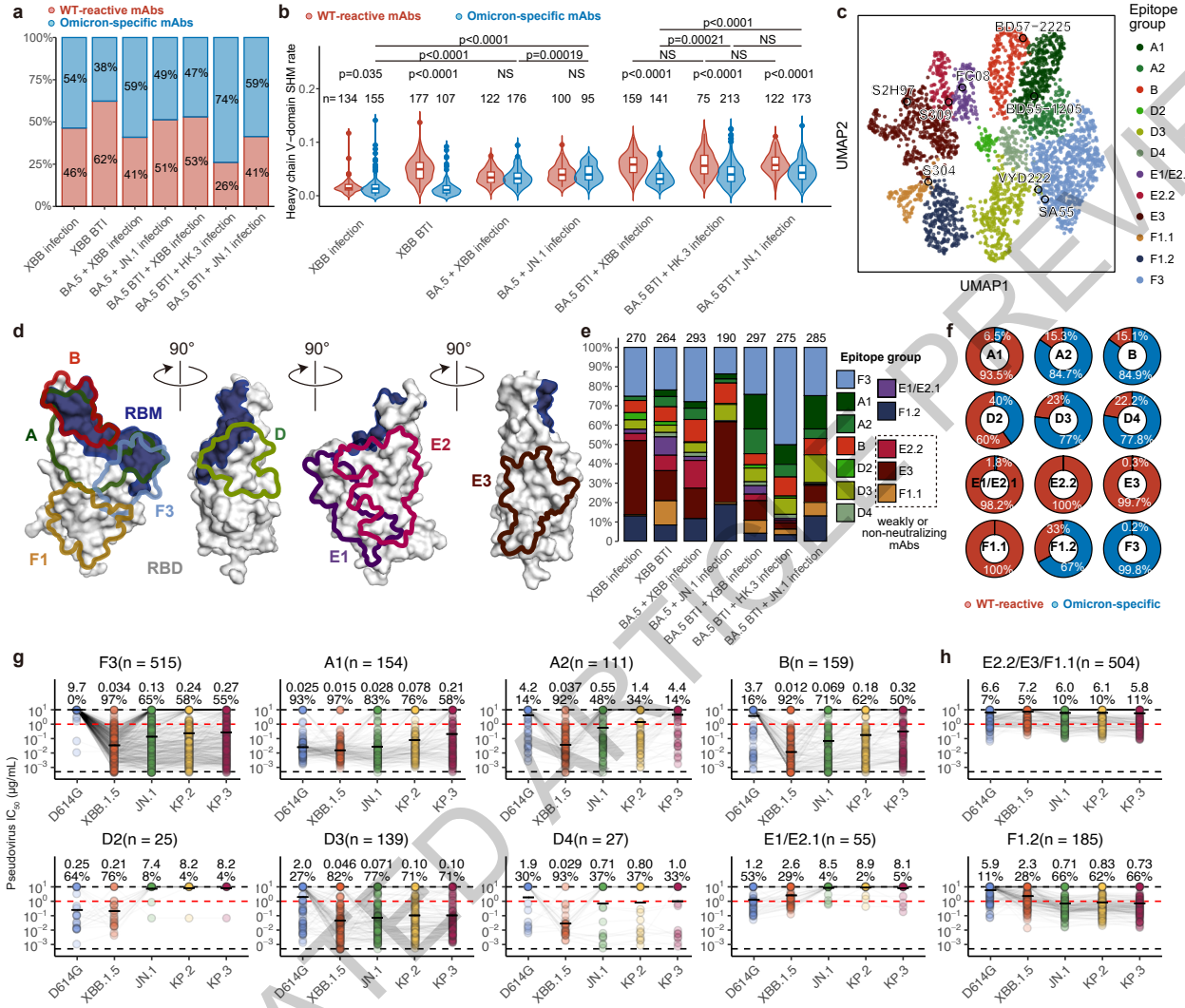

Figure 4

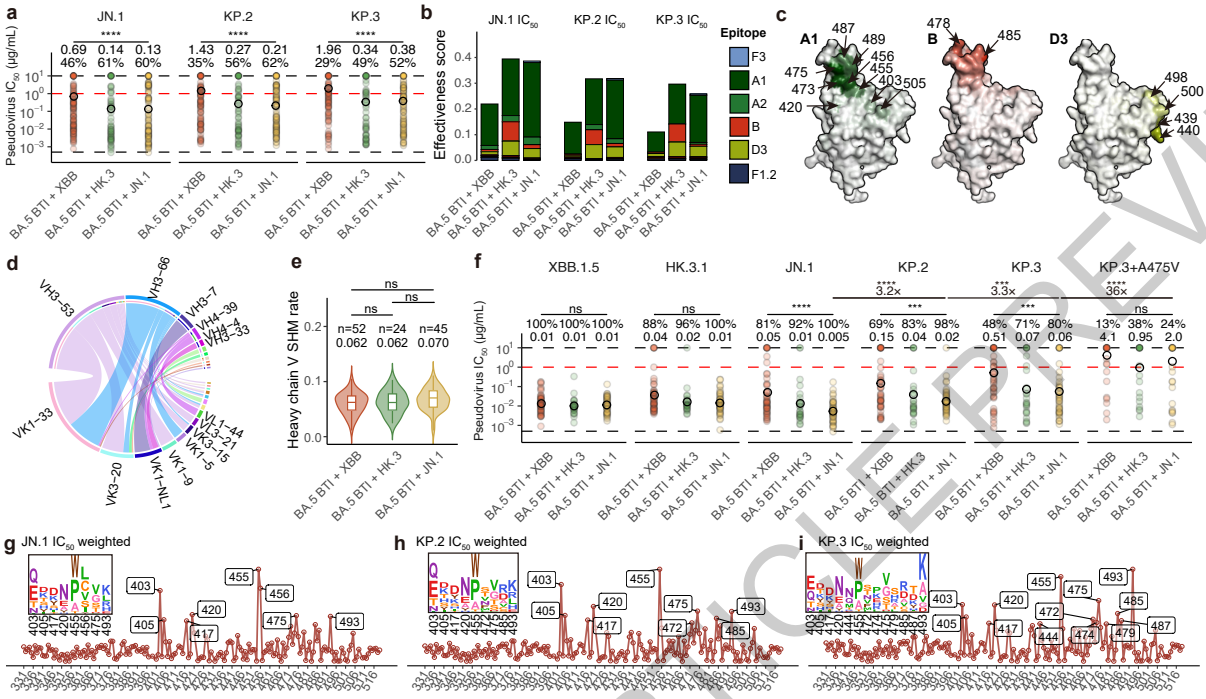

Figure 5

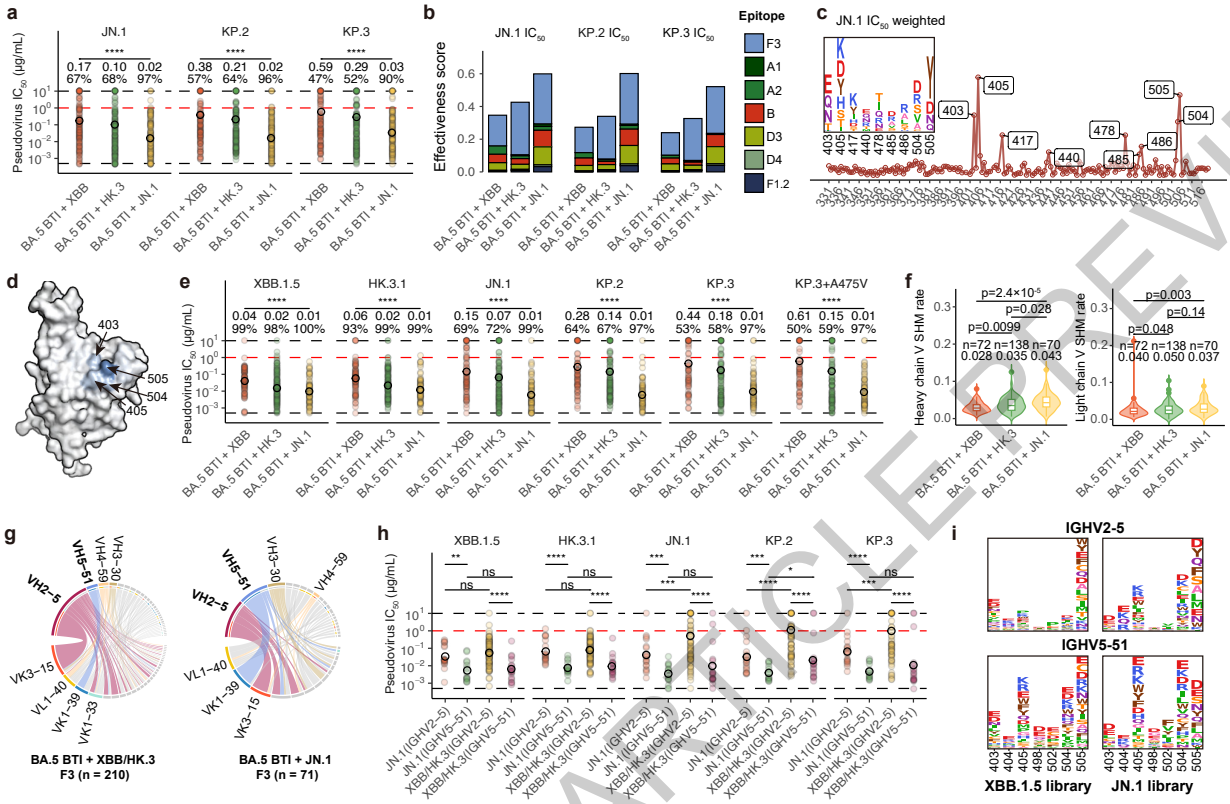

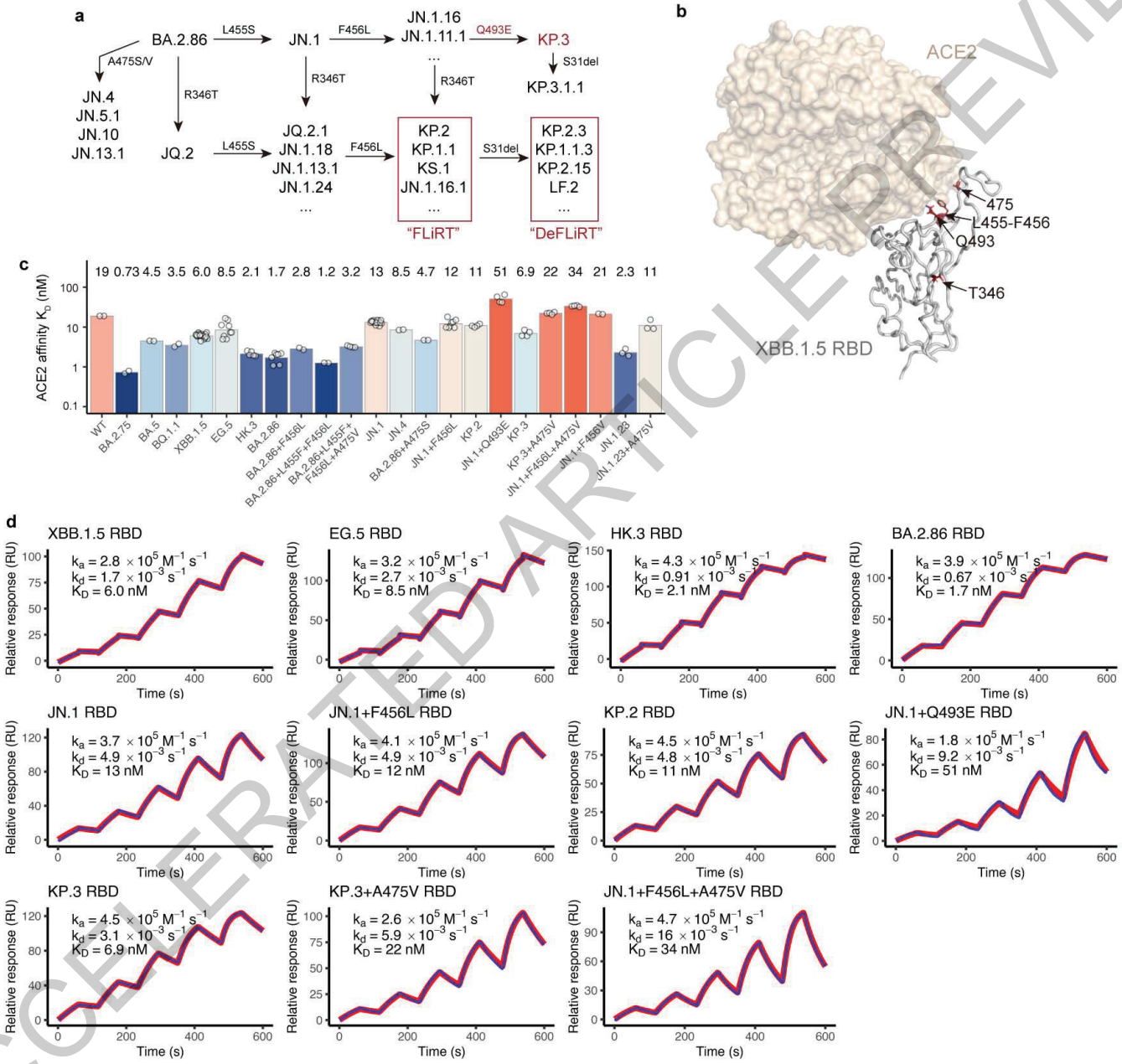

Extended Data Fig. 1

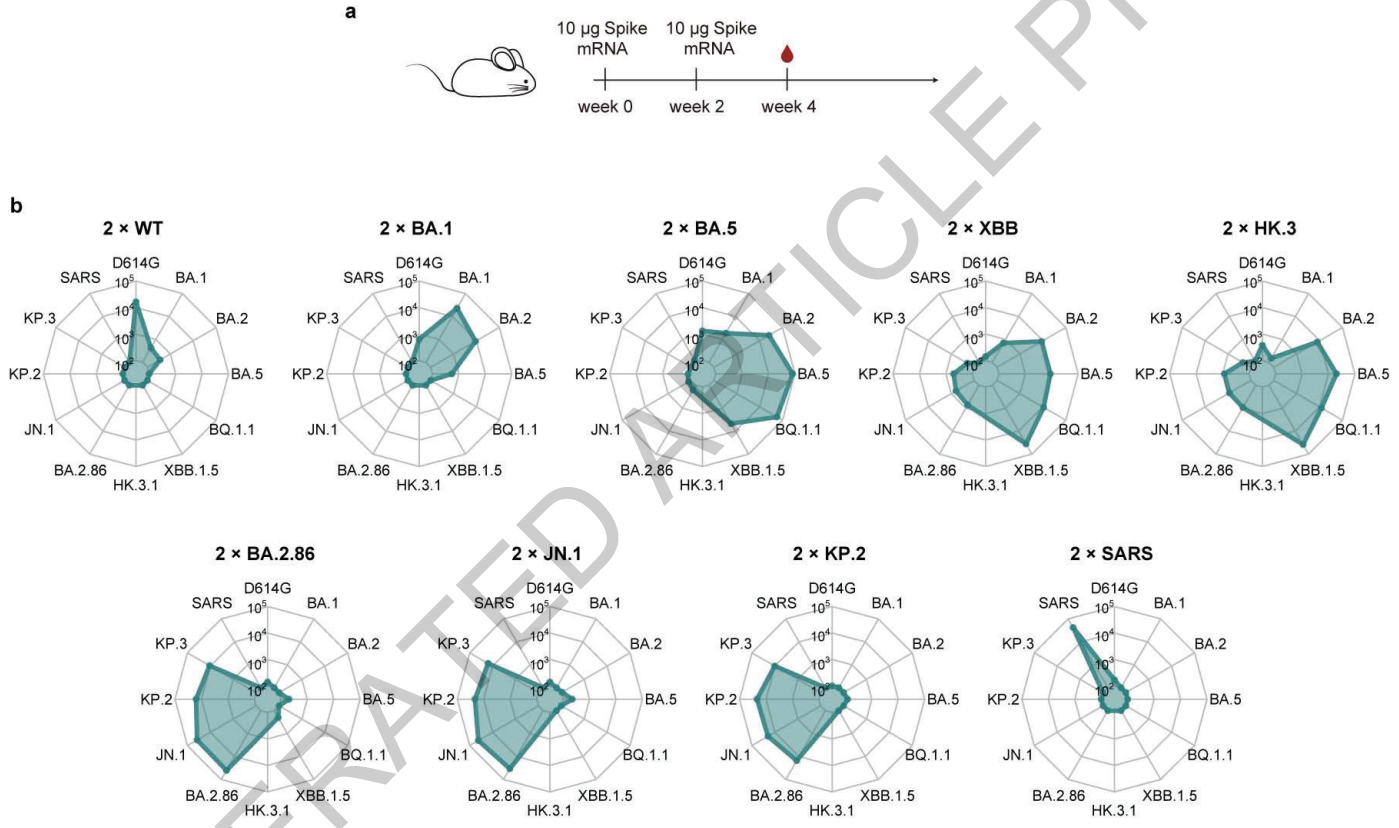

Extended Data Fig. 2

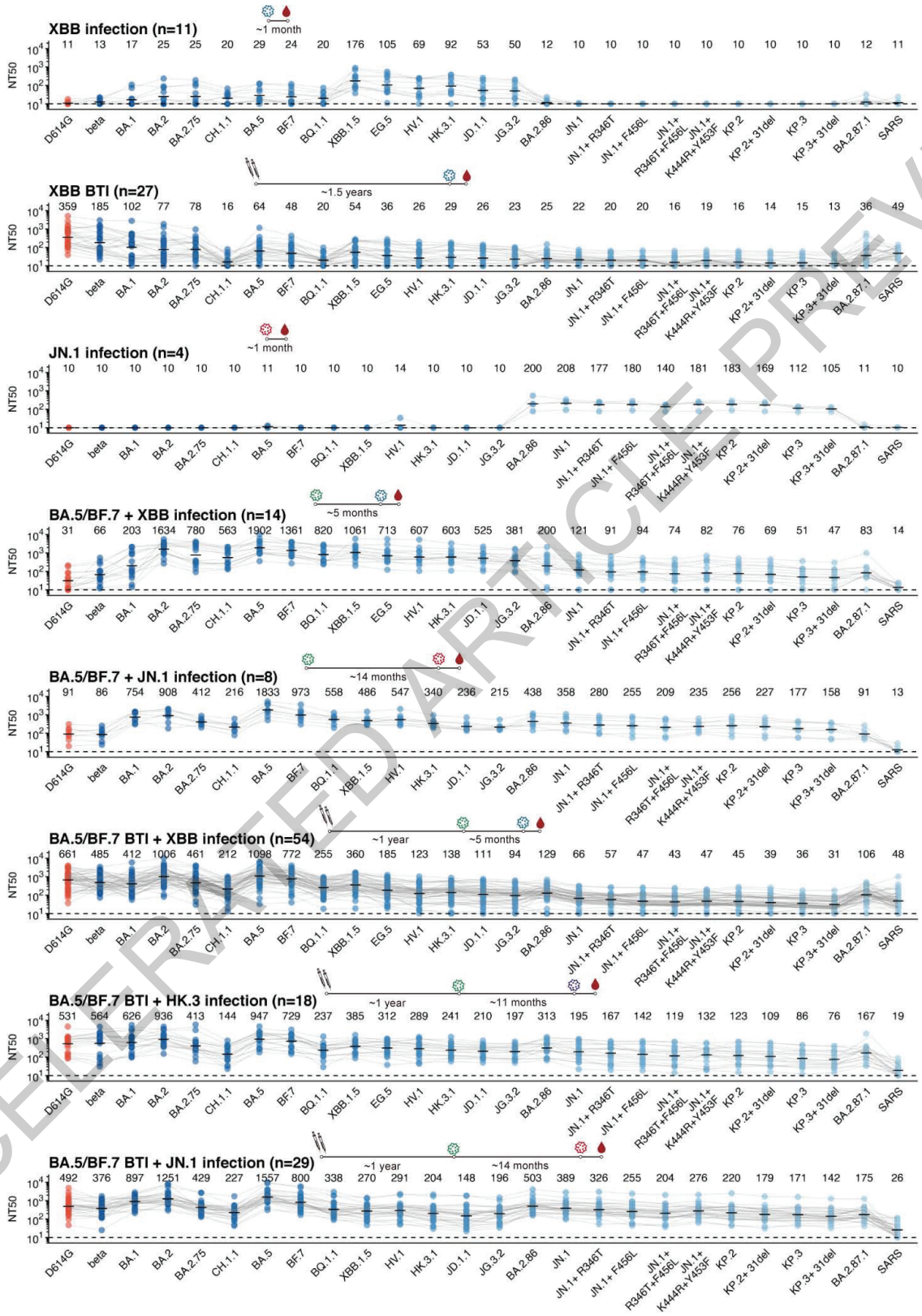

Extended Data Fig. 3

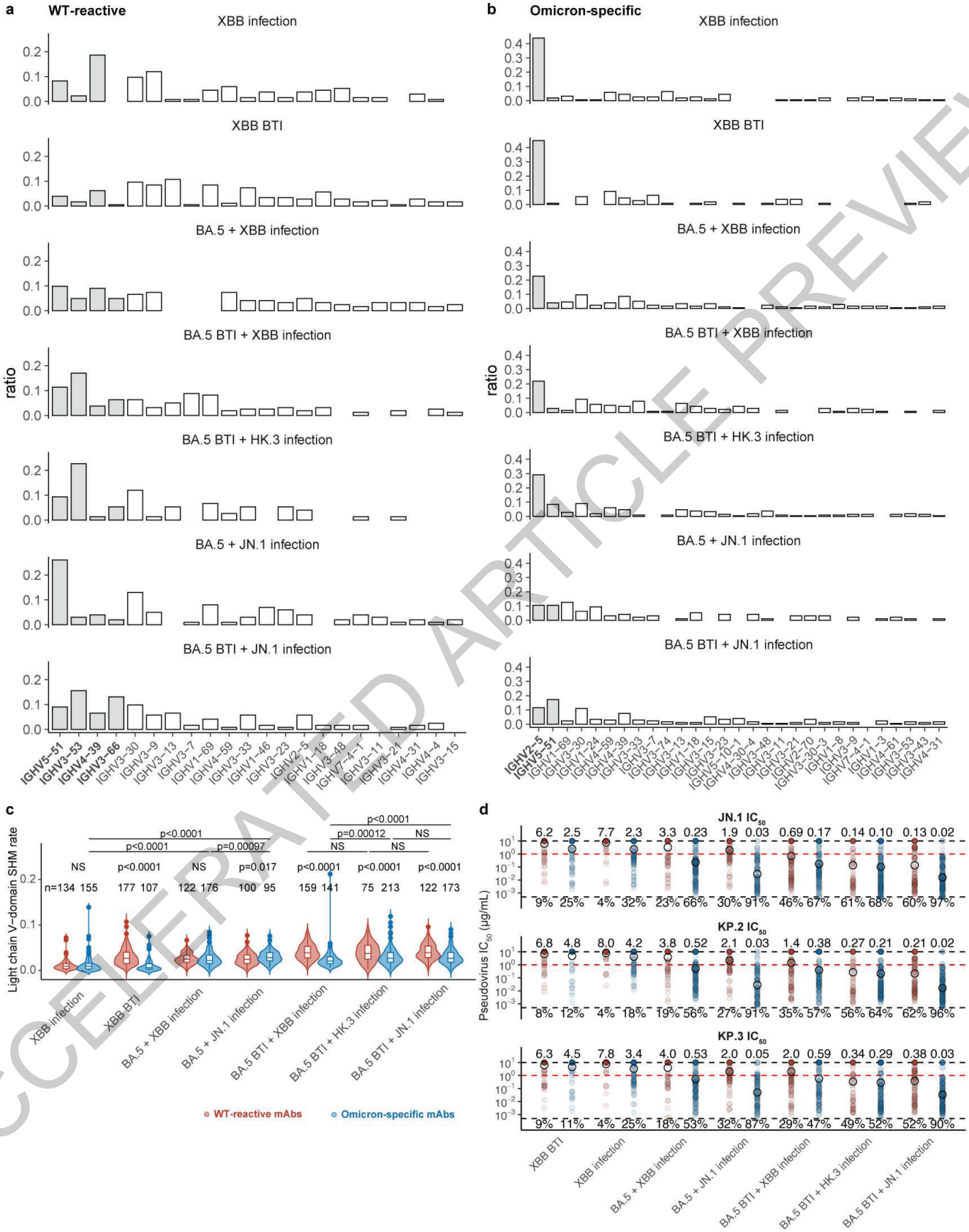

Extended Data Fig. 4

a

antigen	library	variants	detected single mutations
XBB.1.5	lib1	180394	4019
	lib2	122221	4017
	lib1+lib2	302535	4019
JN.1	lib1	159928	3994
	lib2	87824	3994
	lib1+lib2	247679	3999

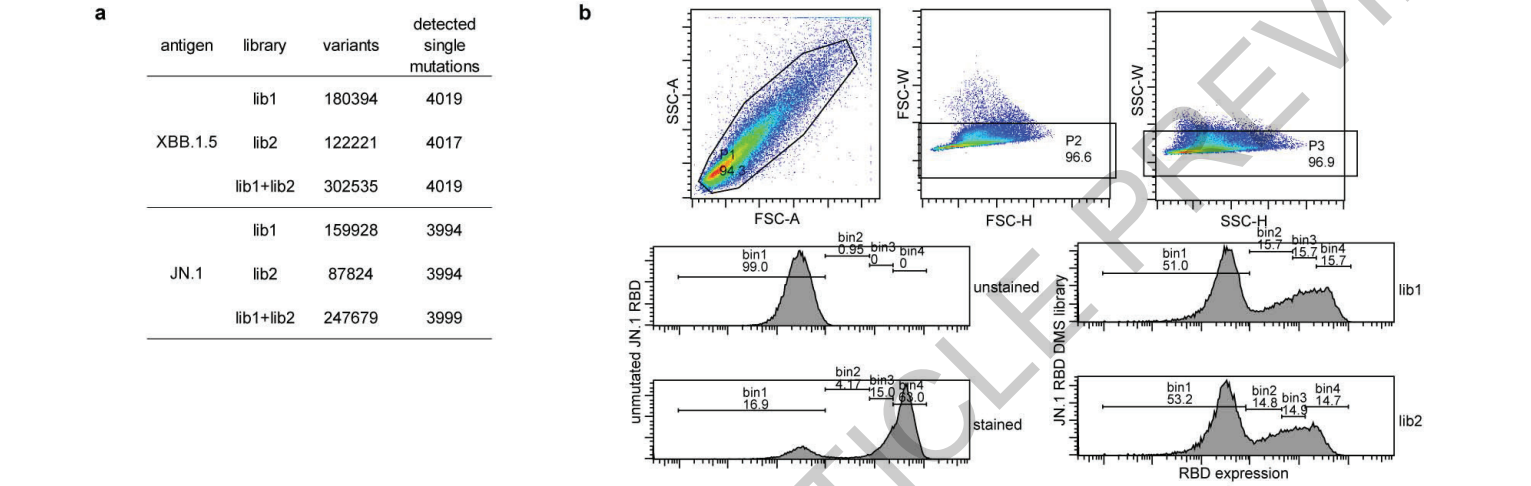

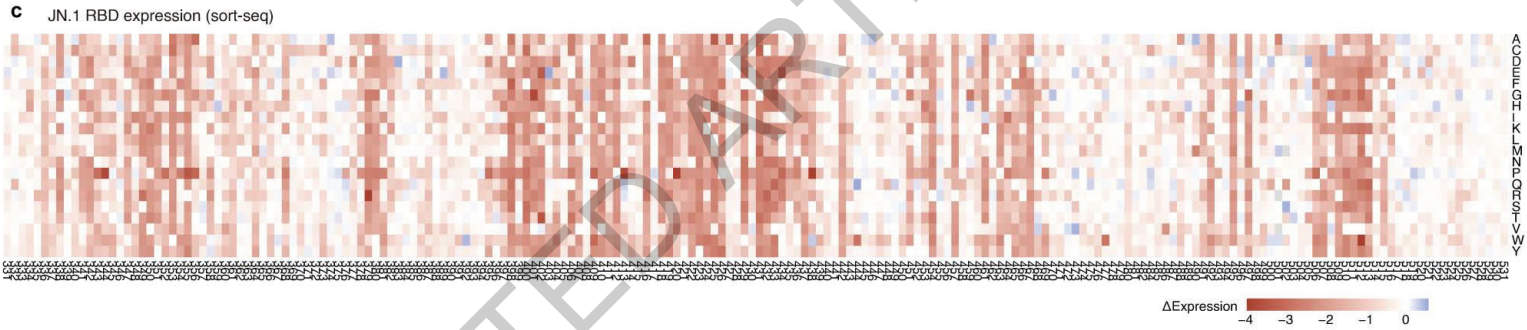

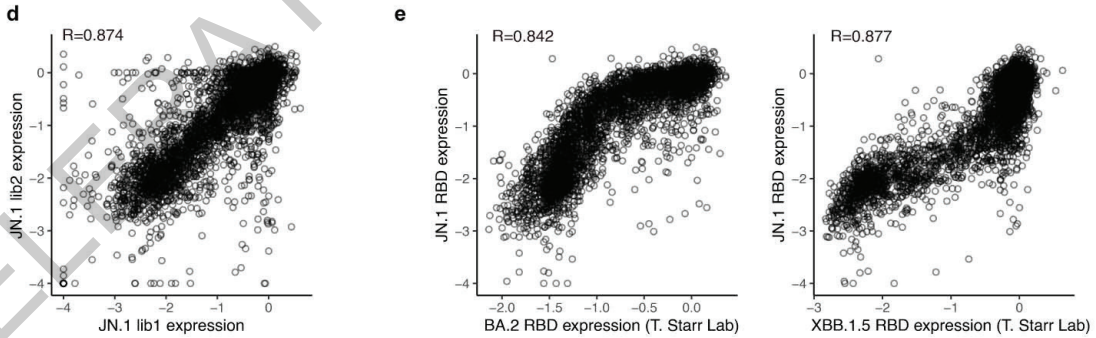

Extended Data Fig. 5

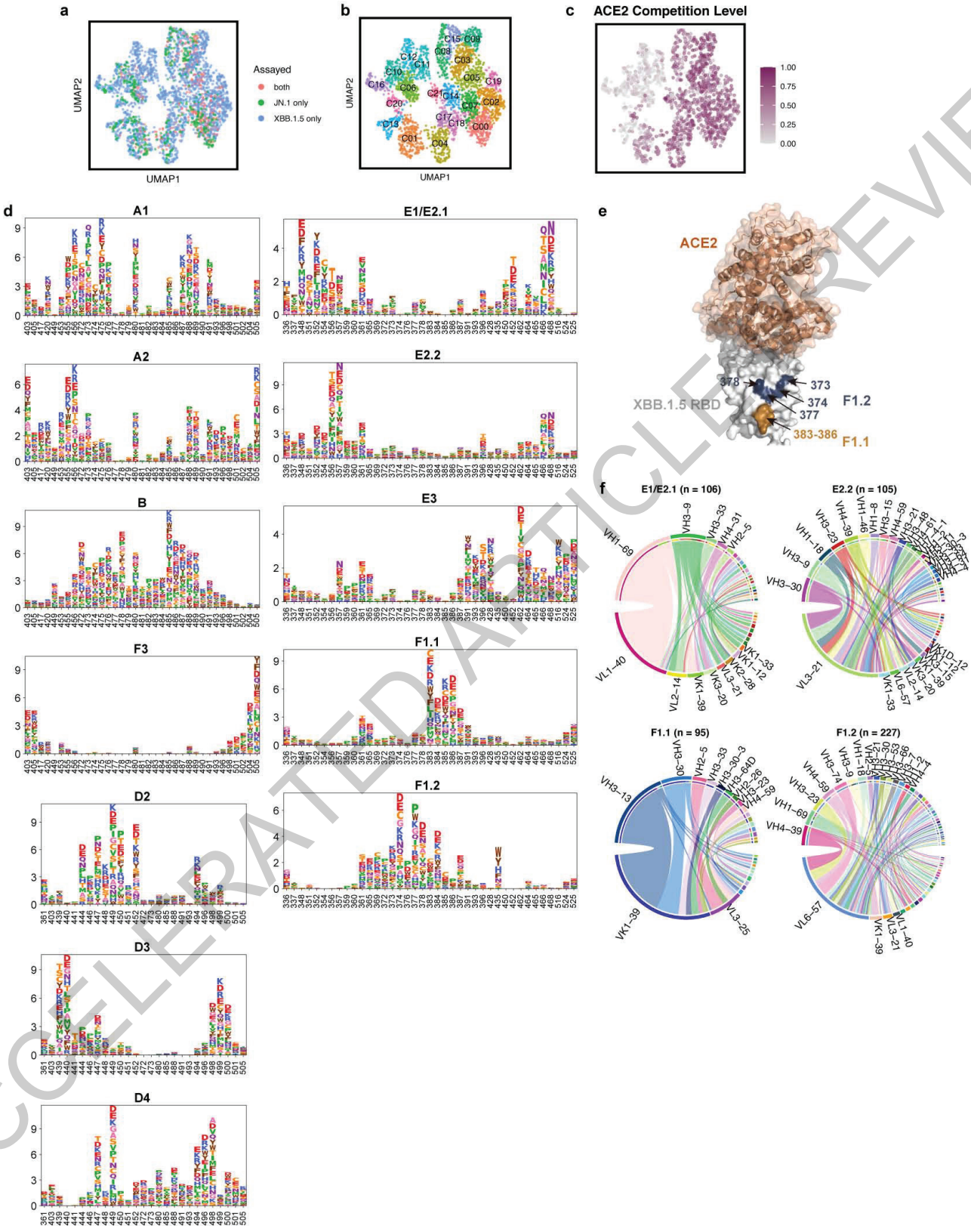

Extended Data Fig. 6

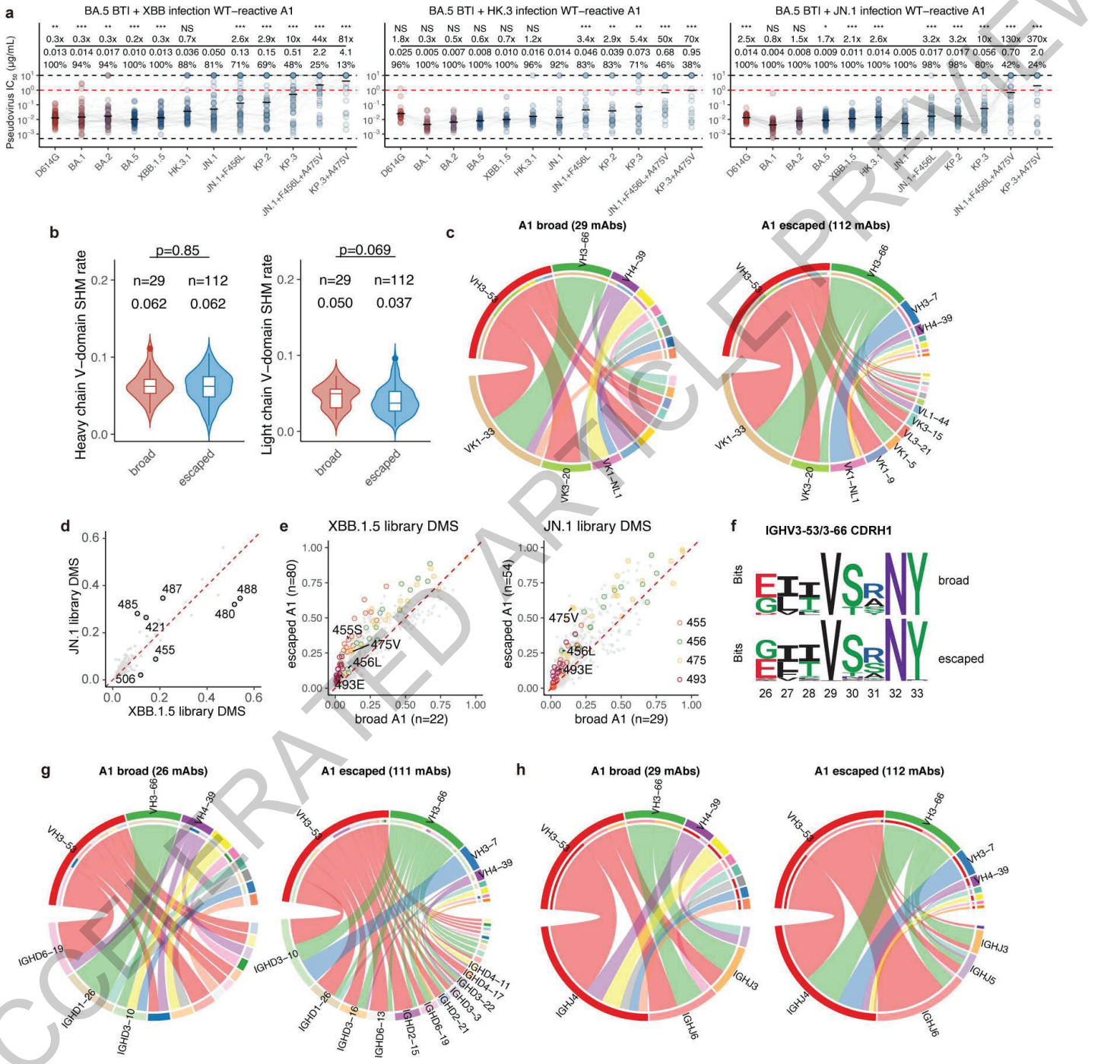

Extended Data Fig. 7

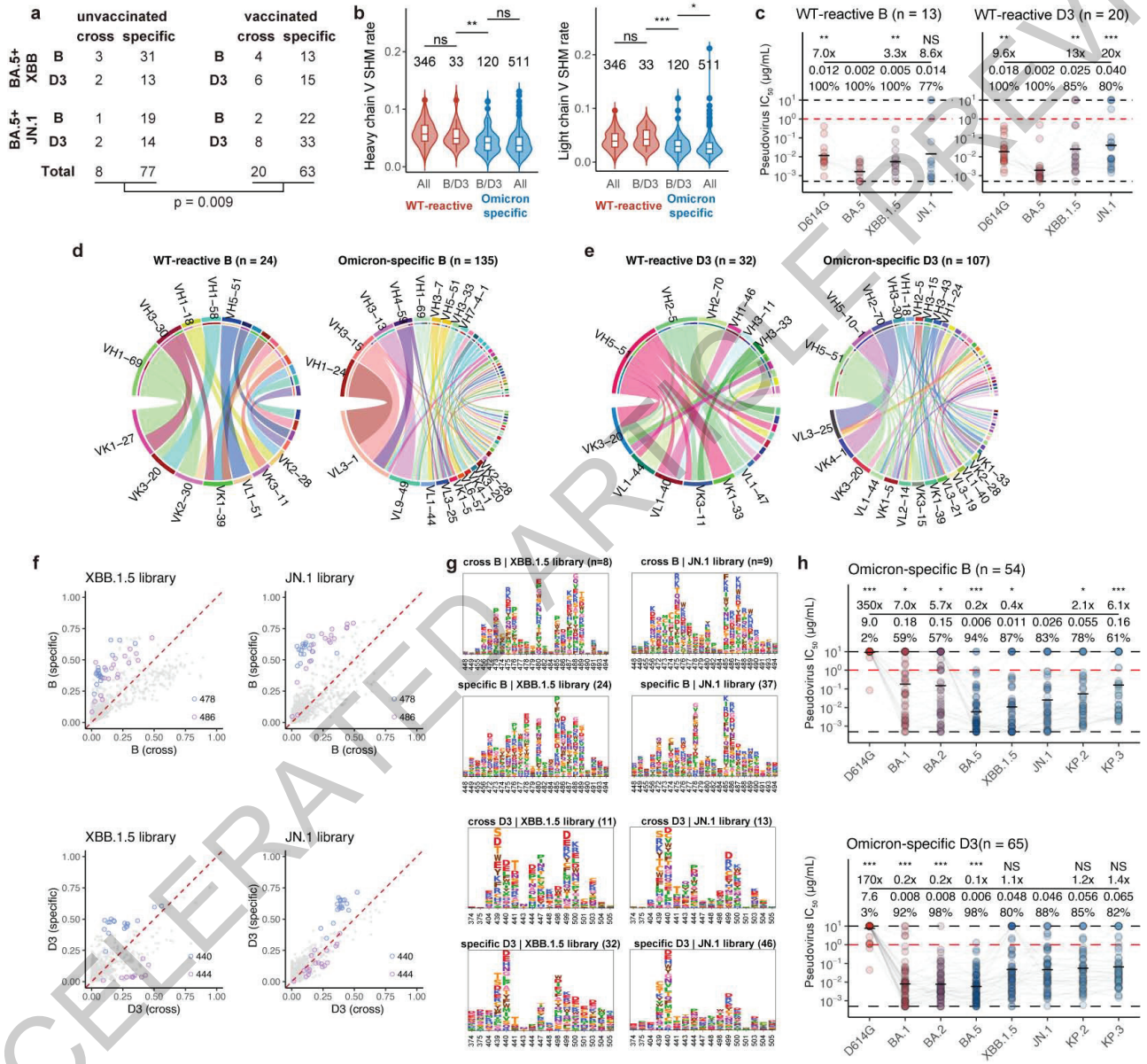

Extended Data Fig. 8

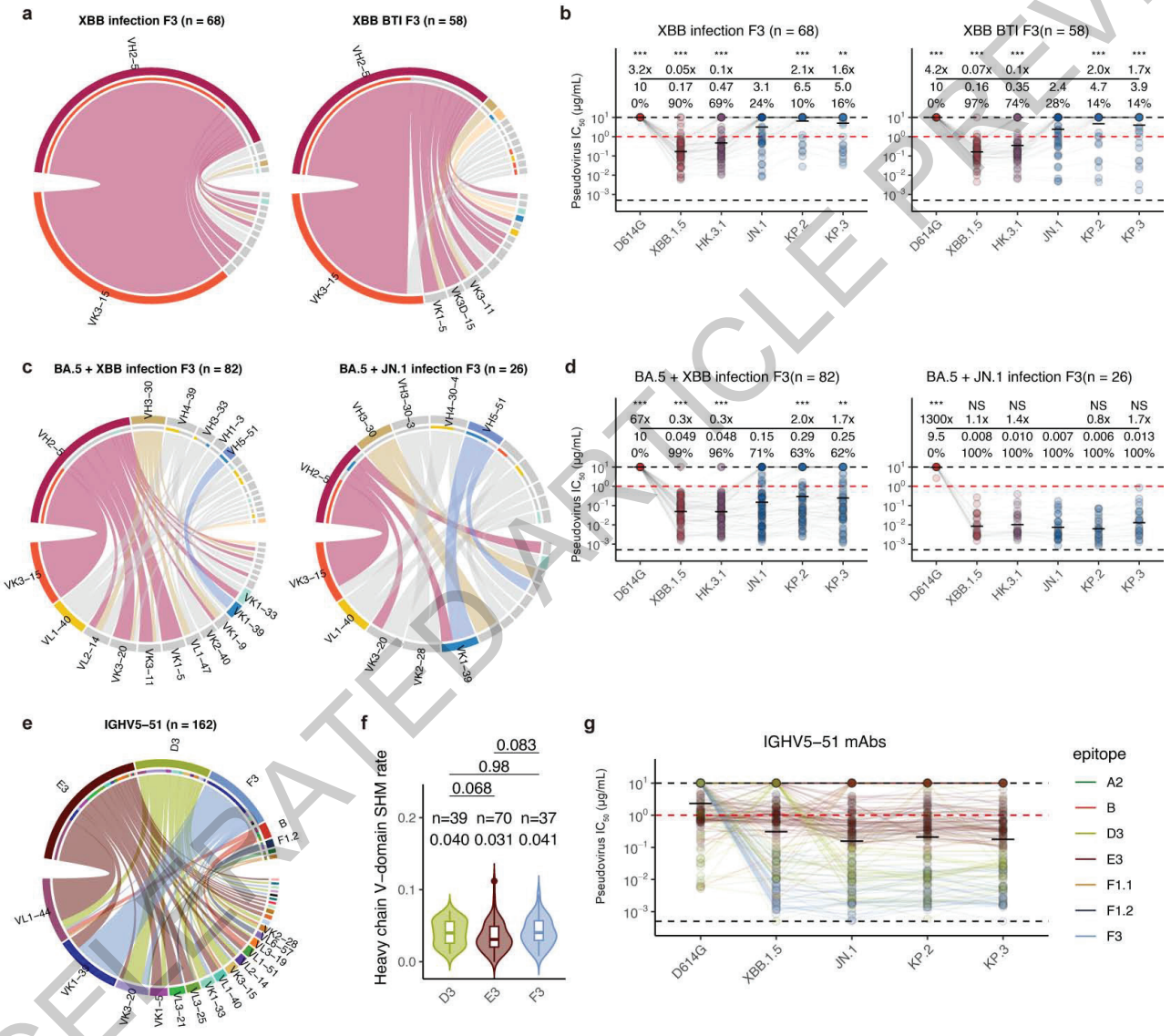

Extended Data Fig. 9

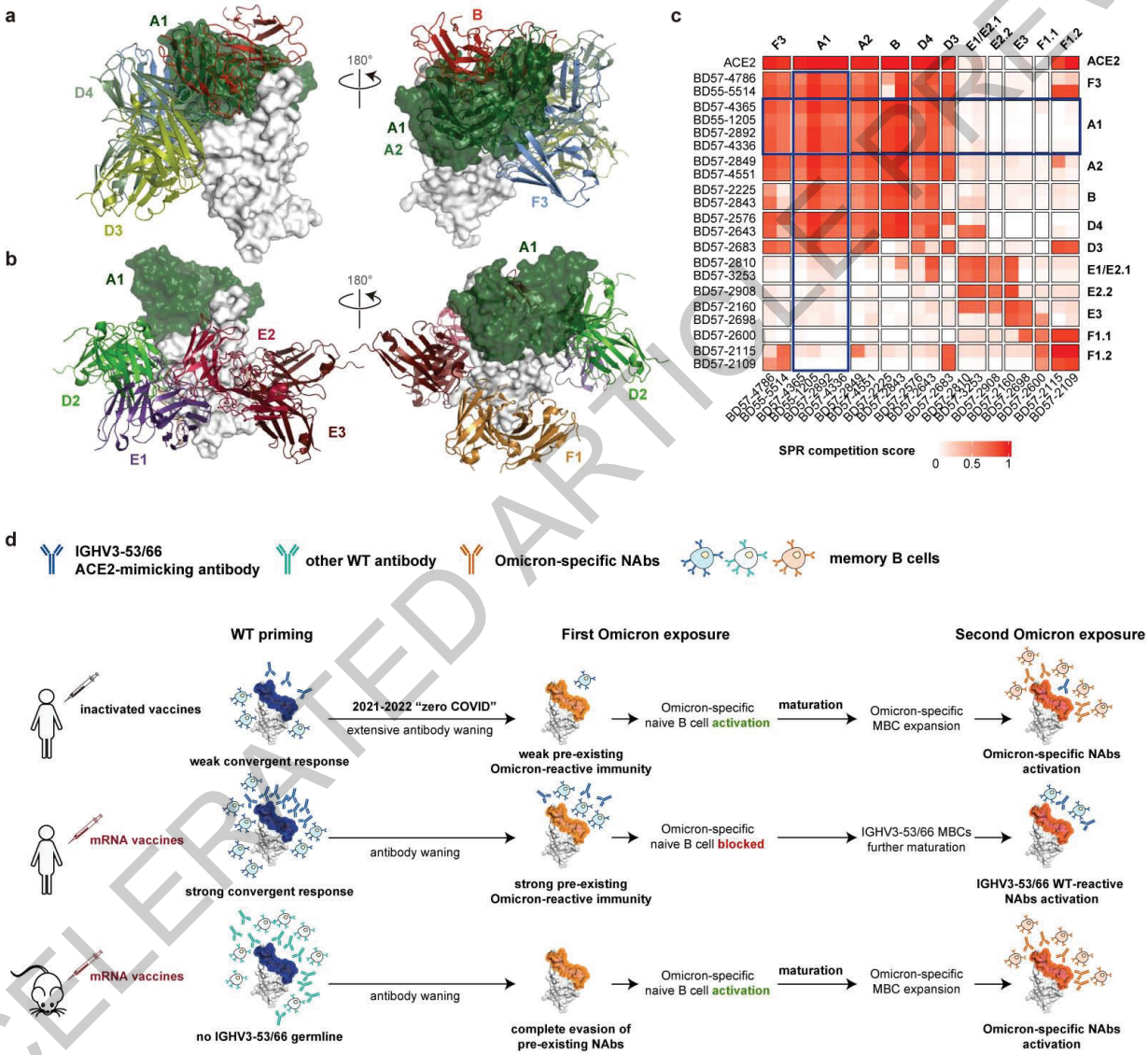

Extended Data Fig. 10

nature portfolio

Corresponding author(s): Yunlong Cao

Last updated by author(s): Oct 3, 2024

Reporting Summary

Nature Portfolio wishes to improve the reproducibility of the work that we publish. This form provides structure for consistency and transparency in reporting. For further information on Nature Portfolio policies, see our Editorial Policies and the Editorial Policy Checklist.

Statistics

For all statistical analyses, confirm that the following items are present in the figure legend, table legend, main text, or Methods section.

n/a	Confirmed	
☐	☒	The exact sample size (*n*) for each experimental group/condition, given as a discrete number and unit of measurement
☐	☒	A statement on whether measurements were taken from distinct samples or whether the same sample was measured repeatedly
☐	☒	The statistical test(s) used AND whether they are one- or two-sided *Only common tests should be described solely by name; describe more complex techniques in the Methods section.*
☒	☐	A description of all covariates tested
☒	☐	A description of any assumptions or corrections, such as tests of normality and adjustment for multiple comparisons
☐	☒	A full description of the statistical parameters including central tendency (e.g. means) or other basic estimates (e.g. regression coefficient) AND variation (e.g. standard deviation) or associated estimates of uncertainty (e.g. confidence intervals)
☐	☒	For null hypothesis testing, the test statistic (e.g. *F*, *t*, *r*) with confidence intervals, effect sizes, degrees of freedom and *P* value noted *Give P values as exact values whenever suitable.*
☒	☐	For Bayesian analysis, information on the choice of priors and Markov chain Monte Carlo settings
☒	☐	For hierarchical and complex designs, identification of the appropriate level for tests and full reporting of outcomes
☒	☐	Estimates of effect sizes (e.g. Cohen's *d*, Pearson's *r*), indicating how they were calculated

Our web collection on statistics for biologists contains articles on many of the points above.

Software and code

Policy information about availability of computer code

Data collection	Pseudovirus neutralization and ELISA data were collected by Multiskan™ FC Microplate Photometer. SPR data was collected by BIAcore 8K Evaluation Software (v4.0.8.20368; GE Healthcare). FACS data was collected by Summit 6.0 (Beckman Coulter).
Data analysis	Neutralization assays data were analyzed using PRISM (v9.0.1) . FACS data were analyzed by FlowJo 10.8. SPR data were analyzed by BIAcore 8K Evaluation Software ((v4.0.8.20368; Cytiva). Sequence alignment of Omicron sublineages was performed by biopython (v1.78); V(D)J sequence data were aligned using Cell Ranger (v6.1.1), The IgBlast program (v1.17.1) and Change-O toolkit (v1.2.0) were utilized to annotate the germline V(D)J genes and detect somatic hypermutation sites in the variable domain of the BCR sequences. Illumina barcodes sequencing data from deep mutational scanning experiments were analyzed using custom scripts (https://github.com/jianfcpku/SARS-CoV-2-reinfection-DMS) and Python package dms_variants (v0.8.9). Custom scripts to analyze the escape mutation profiles data are available at Github (https://github.com/yunlongcaolab/SARS-CoV-2-JN.1-mAbs). We used Python package logomaker (v0.8), R package ggseqlogo (v0.1) and ggplot2 (v3.3.3) for illustration, and Python package python-igraph (v0.9.6), scipy (v1.7.0), scikit-learn (v0.24.2), leidenalg (v0.8.7), umap-learn (v0.5.2) to perform clustering and UMAP.

For manuscripts utilizing custom algorithms or software that are central to the research but not yet described in published literature, software must be made available to editors and reviewers. We strongly encourage code deposition in a community repository (e.g. GitHub). See the Nature Portfolio guidelines for submitting code & software for further information.

Data

Policy information about availability of data

All manuscripts must include a data availability statement. This statement should provide the following information, where applicable:

- Accession codes, unique identifiers, or web links for publicly available datasets
- A description of any restrictions on data availability
- For clinical datasets or third party data, please ensure that the statement adheres to our policy

DMS data and custom scripts can be downloaded at Zenodo (doi: 10.5281/zenodo.13893217) and Github (https://github.com/yunlongcaolab/SARS-CoV-2-JN.1-mAbs). Information of the mAbs involved in this study are included in Supplementary Table 2. We used vdj_GRCh38_alts_ensembl-5.0.0 as the reference of V(D)J alignment, which can be obtained from https://support.10xgenomics.com/single-cell-vdj/software/downloads/latest. PDB 8WRL is used for the structural model of SARS-CoV-2 XBB.1.5 RBD.

Field-specific reporting

Please select the one below that is the best fit for your research. If you are not sure, read the appropriate sections before making your selection.

☒ Life sciences ☐ Behavioural & social sciences ☐ Ecological, evolutionary & environmental sciences

For a reference copy of the document with all sections, see nature.com/documents/nr-reporting-summary-flat.pdf

Life sciences study design

All studies must disclose on these points even when the disclosure is negative.

Sample size	A total of 2000 monoclonal antibodies were produced and characterized in the manuscript. We analyzed all antibodies in hand and the sample size of antibodies in this study was sufficient to reach statistical significance by Wilcoxon rank-sum tests for the differences in SHM rates of mAbs from different cohorts and with different specificities. We collected plasma samples from 54 convalescent individuals with BA.5/BF.7 BTI and XBB infection, 27 with XBB BTI, .18 BA.5/BF.7 BTI and HK.3 infection, and 29 with BA.5/BF.7 BTI + JN.1 infection. Further, we investigated 14 individuals with BA.5/BF.7 and XBB infection, 8 BA.5/BF.7 and JN.1 infection, 11 with XBB infection, and 4 with JN.1 infection, who had no history of vaccination. We immunized 10 mice for each group in animal studies. We analyzed all plasma samples collected and the sample size of plasma could reach statistical significance of NT50 values from neutralization assays by two-tailed Wilcoxon signed-rank test. No sample size calculation was performed.
Data exclusions	51 antibodies were excluded from the statistical analyses due to lack of specificity to at least one of SARS-CoV-2 variant RBD. No plasma sample was excluded from the study.
Replication	Experimental assays were performed in at least two independent experiments according to or exceeding standards in the field. Specifically, we performed mutation screening using two independently constructed mutant libraries. We conducted all neutralization assays, ELISA, and SPR assays in at least two independent experiments. Representative results of replicates are reported.
Randomization	Randomization was not required since we were applying a uniform set of measurements across the panel of monoclonal antibodies and plasma. As this is an observational study, randomization is not relevant.
Blinding	Blinding was not required since we were applying a uniform set of measurements across the panel of monoclonal antibodies and plasma. As this is an observational study, investigators were not blinded.

Reporting for specific materials, systems and methods

We require information from authors about some types of materials, experimental systems and methods used in many studies. Here, indicate whether each material, system or method listed is relevant to your study. If you are not sure if a list item applies to your research, read the appropriate section before selecting a response.

Materials & experimental systems

n/a	Involved in the study
☐	☒ Antibodies
☐	☒ Eukaryotic cell lines
☒	☐ Palaeontology and archaeology
☐	☒ Animals and other organisms
☐	☒ Human research participants
☒	☐ Clinical data
☒	☐ Dual use research of concern

Methods

n/a	Involved in the study
☒	☐ ChIP-seq
☐	☒ Flow cytometry
☒	☐ MRI-based neuroimaging

Antibodies

Antibodies used

ELISA: 0.25 μg/ml goat anti-human IgG(H+L)HRP (JACKSON, 109-035-003)
1 μg/ml H7N9 human IgG1 antibody HG1K (Sino Biologicals, Cat #HG1K) was used as negative control.
FACS: The cells were stained with FITC anti-human CD20 antibody (BioLegend, 302304), Brilliant Violet 421 anti-human CD27 antibody (BioLegend, 302824), PE/Cyanine7 anti-human IgM antibody (BioLegend, 314532), PE/Cyanine7 anti-human IgD antibody(BioLegend, 348210).
All human antibodies were expressed using Expi293F™ (Gibco, A14527) with codon-optimized cDNA and human IgG1 constant regions in house. The detailed sequence could be found in Supplementary material.

Validation

All antibodies were expressed using Expi293F™ with codon-optimized cDNA and human IgG1 constant regions. All antibodies' species and specificity to RBD were validated by ELISA. All antibodies neutralization ability was verified by VSV-based pseudotyped virus assays. Details for all SARS-CoV-2 antibodies evaluated in this study is included in Supplementary Table 2.
Goat anti-human IgG(H+L)HRP (JACKSON, 109-035-003): Based on immunoelectrophoresis and/or ELISA, the antibody reacts with whole molecule human IgG. It also reacts with the light chains of other human immunoglobulins. No antibody was detected against non-immunoglobulin serum proteins. The antibody may cross-react with immunoglobulins from other species.
FITC anti-human CD20 antibody was validated by successful staining and FC analysis according to the manufacturer's website https://www.biolegend.com/en-us/products/fitc-anti-human-cd20-antibody-558 and previous publication: Mishra A, et al. 2021. Cell 184(13):3394-3409.e20
Brilliant Violet 421 anti-human CD27 antibody was validated by successful staining and FC analysis according to the manufacturer's website https://www.biolegend.com/en-us/products/brilliant-violet-421-anti-human-cd27-antibody-7276 and previous publication Dugan HL, et al. 2021. Immunity. 54(6):1290-1303
PE/Cyanine7 anti-human IgM antibody was validated by successful staining and FC analysis according to the manufacturer's website https://www.biolegend.com/en-us/products/pe-cyanine7-anti-human-igm-antibody-12467 and previous publication: Shehata L, et al 2019. Nat Commun. 10:1126
PE/Cyanine7 anti-human IgD antibody was validated by successful staining and FC analysis according to the manufacturer's website https://www.biolegend.com/en-us/products/pe-cyanine7-anti-human-igd-antibody-6996 and previous publication: Ahmed R et al. 2019. Cell. 177(6):1583-1599.

Eukaryotic cell lines

Policy information about cell lines

Cell line source(s)

Monoclonal antibody expression: Expi293F™ (Gibco, A14527);
Yeast display: EBY100 (ATCC MYA-4941);
Pseudutyped virus neutralization assay: Huh-7 (JCRB 0403) ;
Authentic virus neutralizing assay:Vero(ATCC CCL-81);
293T(ATCC, CRL-3216);

Authentication

Expi293F™ (Gibco, A14527):Morphology(https://www.thermofisher.com/document-connect/document-connect.html?url=https://assets.thermofisher.com/TFS-Assets%2Fcertificate%2FFRK%2FCOA%2FCOA_100044202_275162_1.pdf);
EBY100 (ATCC MYA-4941):Whole-genome Sequencing(https://www.atcc.org/products/mya-4941);
Huh-7 (JCRB 0403):Morphology(https://cellbank.nibiohn.go.jp/~cellbank/en/search_res_det.cgi?ID=385);
Vero(ATCC CCL-81):Morphology(https://www.atcc.org/products/ccl-81#related-products);
293T(ATCC, CRL-3216):STR profiling(https://www.atcc.org/products/crl-3216)

Mycoplasma contamination

Not tested for mycoplasma contamination;

Commonly misidentified lines
(See ICLAC register)

No commonly misidentified cell lines were used in the study.

Animals and other organisms

Policy information about studies involving animals; ARRIVE guidelines recommended for reporting animal research

Laboratory animals	Female,six to eight-week-old BALB/c mice were used in this study
Wild animals	No wild animals were used.
Field-collected samples	No field-collected samples were used.
Ethics oversight	Animal experiments were carried out under study protocols approved by Institute of Biophysics, Chinese Academy of Sciences (SYXK2023300) and HFK Biologics (HFK-AP-20210930).

Note that full information on the approval of the study protocol must also be provided in the manuscript.

Human research participants

Policy information about studies involving human research participants

Population characteristics	We collected plasma samples from 54 convalescent individuals with BA.5/BF.7 BTI and XBB infection, 27 with XBB BTI, .18 BA.5/BF.7 BTI and HK.3 infection, and 29 with BA.5/BF.7 BTI + JN.1 infection. Further, we investigated 14 individuals with BA.5/BF.7 and XBB infection, 8 BA.5/BF.7 and JN.1 infection, 11 with XBB infection, and 4 with JN.1 infection, who had no history of vaccination. The gender, age, vaccination status, infection time, and sampling time were listed in Supplementary Table 1.
Recruitment	Patients were recruited on the basis of SARS-CoV-2 vaccinations, and known SARS-CoV-2 infections indicated by SARS-CoV-2 PCR or antigen tests. The strains that infected the participants were inferred from corresponding regional epidemiological data, as described in the online methods. The exclusion criteria for the study included individuals with HIV or other debilitating diseases, as well as immunocompromised individuals.
Ethics oversight	Blood samples from vaccinated or unvaccinated individuals were obtained under study protocols approved by Beijing Ditan Hospital, Capital Medical University (Ethics committee archiving No. LL-2021-024-02) and the Tianjin Municipal Health Commission, and the Ethics Committee of Tianjin First Central Hospital (Ethics committee archiving No. 2022N045KY). All participants have provided written informed consent for the collection of information, storage and use of their clinical samples for research purposes, and publication of data generated from this study.

Note that full information on the approval of the study protocol must also be provided in the manuscript.

Flow Cytometry

Plots

Confirm that:

☒ The axis labels state the marker and fluorochrome used (e.g. CD4-FITC).

☒ The axis scales are clearly visible. Include numbers along axes only for bottom left plot of group (a 'group' is an analysis of identical markers).

☒ All plots are contour plots with outliers or pseudocolor plots.

☒ A numerical value for number of cells or percentage (with statistics) is provided.

Methodology

Sample preparation	Whole blood sample were diluted 1:1 with PBS+2% FBS (Gibco) and subjected to Ficoll (Cytiva) gradient centrifugation. Plasma was collected from upper layer. Cells were collected at the interface and further prepared by centrifugation, red blood cells lysis (Invitrogen eBioscience) and washing steps. Samples were stored in FBS (Gibco) with 10% DMSO (Sigma) in liquid nitrogen if not used for downstream process immediately. Cryopreserved PBMCs were thawed in PBS+2% FBS. CD19+ B cells were enriched from PBMCs using EasySep Human CD19 Positive Selection Kit II (STEMCELL, 17854). Following enrichment, 1x10^6 B cells in 100µl buffer were incubated with a panel of antibodies including 3µl FITC anti-human CD20 antibody (BioLegend, 302304), 3.5µl Brilliant Violet 421 anti-human CD27 antibody (BioLegend, 302824), 2µl PE/Cyanine7 anti-human IgD antibody (BioLegend, 348210) and 2µl PE/Cyanine7 anti-human IgM antibody (BioLegend, 314532). Additionally, fluorophore or oligonucleotide conjugated RBD were added. For FACS, 0.013µg of biotinylated XBB.1.5, HK.3, or JN.1 RBD protein (customized from Sino Biological) conjugated with PE-streptavidin (BioLegend, 405204) and APC-streptavidin (BioLegend, 405207), and 0.013µg of WT biotinylated RBD protein (Sino Biological, 40592-V27H-B) conjugated with BV605-streptavidin (BioLegend, 405229) were added. For sequencing, XBB.1.5, HK.3, or JN.1 biotinylated RBD protein conjugated with TotalSeq™-C0971 Streptavidin (BioLegend, 405271) and TotalSeq™-C0972 Streptavidin (BioLegend, 405273), WT biotinylated RBD protein conjugated with TotalSeq™-C0973 Streptavidin (BioLegend, 405275) and TotalSeq™-C0974 Streptavidin (BioLegend, 405277) and biotinylated Ovalbumin (Sino Biological) conjugated with TotalSeq™-C0975 Streptavidin (BioLegend, 405279) were added. After incubation and washing steps, 5µl of 7-AAD (Invitrogen, 00-6993-50) was included for dead cell exclusion.
Instrument	Moflo Astrios EQ (BeckMan Coulter)

Software	Summit 6.0 (Beckman Coulter) for cell sorting; FlowJo 10.8 for data analysis.
Cell population abundance	Detailed abundance data are shown in the Supplementary Information.
Gating strategy	Cells negative for 7-AAD, IgM and IgD, but positive for CD20, CD27 and XBB.1.5, HK.3 or JN.1 RBD were sorted, the gating strategy is provided in the Supplementary Information

☒ Tick this box to confirm that a figure exemplifying the gating strategy is provided in the Supplementary Information.